

ESTIMATING THE ARRIVAL TIME OF EARTH-DIRECTED CORONAL MASS EJECTIONS AT IN SITU SPACECRAFT USING COR AND HI OBSERVATIONS FROM STEREO

WAGEESH MISHRA AND NANDITA SRIVASTAVA

Udaipur Solar Observatory, Physical Research Laboratory, P.O. Box 198, Badi Road, Udaipur 313 001, India; wageesh@prl.res.in

Received 2012 October 22; accepted 2013 May 14; published 2013 July 8

ABSTRACT

Predicting the arrival time and transit speed of coronal mass ejections (CMEs) near the Earth is critical to understanding the solar-terrestrial relationship. Even though *STEREO* observations now provide multiple views of CMEs in the heliosphere, the true speeds derived from stereoscopic reconstruction of SECCHI coronagraph data are not quite sufficient for accurate forecasting of the arrival time at Earth of a majority of CMEs. This uncertainty is due to many factors that change CME kinematics, such as the interaction of two or more CMEs or the interaction of CMEs with the pervading solar wind. In order to understand the propagation of CMEs, we have used the three-dimensional triangulation method on SECCHI coronagraph (COR2) images and geometric triangulation on the *J*-maps constructed from Heliospheric Imagers HI1 and HI2 data for eight Earth-directed CMEs observed during 2008–2010. Based on the reconstruction, and implementing the drag-based model for the distance where the CMEs could not be tracked unambiguously in the interplanetary (IP) medium, the arrival time of these CMEs have been estimated. These arrival times have also been compared with the actual arrival times as observed by in situ instruments. The analysis reveals the importance of heliospheric imaging for improved forecasting of the arrival time and direction of propagation of CMEs in the IP medium.

Key words: shock waves – solar-terrestrial relations – solar wind – Sun: coronal mass ejections (CMEs) – Sun: heliosphere

Online-only material: color figures

1. INTRODUCTION

Coronal mass ejections (CMEs) are huge magnetized plasma eruptions from the Sun into interplanetary (IP) space. CMEs are observed in a coronagraphic field of view (FOV) as an outward motion of new discrete, bright, white-light features over a timescale of tens of minutes (Hundhausen et al. 1984). CMEs are known to be the potential drivers of geomagnetic storms and many space weather effects (Gosling et al. 1990; Richardson et al. 2001; Echer et al. 2008). Heliospheric counterparts of CMEs are called interplanetary coronal mass ejections (ICMEs; Zhao 1992; Dryer 1994). The precise relation between CMEs and ICMEs is not well understood because there is no unique signature identifying an ICME. Although the term ICME was originally coined to distinguish between remote sensing observations of CMEs near the Sun by coronagraphs and their near-Earth observations by in situ spacecraft, in the present *Solar TErrestrial RElations Observatory* (*STEREO*) era, where CMEs can be tracked from near the Sun to the Earth and beyond, the term ICME has become redundant (Webb & Howard 2012). Therefore, in this paper we use the term CME throughout to refer to both CMEs and ICMEs.

Most of the studies carried out to calculate the travel time of CMEs from the Sun to the Earth have suffered from a lot of assumptions regarding the geometry and evolution of a CME in the IP medium (Howard & Tappin 2009a; Vršnak et al. 2010). Earth-directed CMEs with a southward IP magnetic field component interact with the magnetosphere at the dayside magnetopause. In this interaction, solar wind energy is transferred to the magnetosphere, primarily via magnetic reconnection that produces non-recurrent geomagnetic storms (Dungey 1961). The rate of magnetic reconnection depends on the magnitude of the IP convective electric field ($V \times B$; Gosling et al. 1991). Also, it has been shown that 83% of

intense geomagnetic storms are due to CMEs (Zhang et al. 2007). Therefore, it is necessary to estimate the arrival time and transit speeds of CMEs near the Earth well in advance in order to predict a majority of space weather events.

With the launch of the *SOlar and Heliospheric Observatory* (*SOHO*), studies of the evolution of CMEs were carried out which primarily focused on observations by the Large Angle and Spectrometric COronagraph (LASCO; Brueckner et al. 1995) on board *SOHO*. Furthermore, studies were devoted to the in situ identification of CMEs near the Earth by *Advanced Composition Explorer* (*ACE*; Stone et al. 1998) and *WIND* (Ogilvie et al. 1995) combined with modeling efforts (Wood et al. 1999; Andrews et al. 1999). Understanding of the kinematics of CMEs was based on two point measurements, one near the Sun up to a distance of $30 R_{\odot}$ using coronagraph images, and the other near the Earth using in situ instruments. Using the LASCO images, one could also estimate projected speeds of CMEs, although we lacked information about the true speed and direction of the Earth-directed CMEs.

An empirical CME arrival (ECA) model has been developed by Gopalswamy et al. (2001). These authors considered that a CME has an average acceleration up to a distance of 0.7–0.95 AU. After the cessation of acceleration, a CME is assumed to move with a constant speed. Gopalswamy et al. (2001) found that the average acceleration has a linear relationship with the initial plane-of-sky speed of the CME. The ECA model has been able to predict the arrival time of CMEs to within an error of approximately ± 35 hr with an average error of 11 hr. Later, an empirical shock arrival (ESA) model was developed that was able to predict the arrival time of CMEs to within an error of approximately ± 30 hr with an average error of 12 hr (Gopalswamy et al. 2005). The ESA model is a modified version of the ECA model in which a CME is considered to be the driver of magnetohydrodynamic (MHD) shocks. The other

assumption is that fast mode MHD shocks are similar to gas dynamic shocks. Therefore, the gas dynamic piston-shock relationship is utilized in the ESA model. Various models have been developed to forecast the CME arrival time at 1 AU, based on an empirical relationship between measured projected speeds and arrival time characteristics of various events (e.g., Gopalswamy et al. 2001; Vršnak & Gopalswamy 2002; Schwenn et al. 2005). Also, the analytical drag-based model (DBM; e.g., Vršnak & Žic 2007; Lara & Borgazzi 2009; Vršnak et al. 2010) and numerical MHD simulation models (e.g., Odstrcil et al. 2004; Manchester et al. 2004; Smith et al. 2009) have been developed. The efficacy of all these models in predicting CME arrival times has been analyzed in various studies (e.g., Dryer et al. 2004; Feng et al. 2009; Smith et al. 2009). These studies show that the predicted arrival time is usually within an error of ± 10 hr but sometimes the errors can be larger than 24 hr. Many studies have also shown that CMEs interact significantly with the ambient solar wind as they propagate in the IP medium, resulting in the acceleration of slow CMEs and the deceleration of fast CMEs toward the ambient solar wind speed (Lindsay et al. 1999; Gopalswamy et al. 2000, 2001; Yashiro et al. 2004; Manoharan 2006; Vršnak & Žic 2007).

After the launch of twin *STEREO* (Kaiser et al. 2008) spacecraft, three dimensional (3D) aspects of CMEs could be studied for the first time using its Sun Earth Connection Coronal and Heliospheric Investigation (SECCHI; Howard et al. 2008) coronagraph (COR) and Heliospheric Imager (HI) data. This is because the angular separation between the *STEREO* spacecraft and the Sun–Earth line provides observers with two different viewpoints for; the coronagraph and heliospheric images which are always projections on the plane of sky. This led to the development of various 3D reconstruction techniques (viz., tie-pointing: Inhester 2006; forward modeling: Thernisien et al. 2009; polarization ratio: Moran & Davila 2004). Also, several other methods were developed that are derivatives of the tie-pointing method: the 3D height–time technique (Mierla et al. 2008), local correlation tracking and triangulation (Mierla et al. 2009), and triangulation of the center of mass (Boursier et al. 2009). These methods have been devised to estimate the true heliographic coordinates of CMEs in the COR FOV. However, the estimation of the true speeds of CMEs using a 3D reconstruction method in the coronagraphic (COR2) FOV is often not sufficient for accurately predicting the arrival time of CMEs near the Earth. This result is due to significant changes in the CME dynamics over different segments of the CME’s journey through the IP medium. This may occur either due to varying ambient solar wind conditions or CME–CME interactions in the IP medium. The kinematics of CMEs over a range of heliocentric distances and their interaction in the IP medium has been investigated by exploiting *STEREO*/HI observations (e.g., Harrison et al. 2012; Liu et al. 2012; Lugaz et al. 2012). Also, Davis et al. (2009) showed that the apparent acceleration and deceleration noted in the elongation variation of a CME from one *STEREO* view point can be used to obtain its kinematics and arrival time. Temmer et al. (2011) implemented the “corrected” harmonic mean method to estimate the kinematics of CMEs and compared these to the kinematics of the simulated background solar wind from the 3D MHD model. Byrne et al. (2010) implemented the elliptical tie-pointing technique on the COR and HI observations and quantified the angular width and deflecting trajectory of a CME. In their study, the derived kinematics were used as inputs in the ENLIL (Odstrčil & Pizzo 1999) model to predict the arrival

time of a CME at the first Lagrangian point (L1) near the Earth. Maloney & Gallagher (2010) studied the 3D kinematics of CMEs in the inner heliosphere using *STEREO* observations and pointed out different forms of drag force for fast and slow CMEs. The finding that CMEs near the Sun have a large range of speeds, typically between 100 and 2500 km s⁻¹ (Yashiro et al. 2004), but a narrower range of speeds, typically between 300 and 1000 km s⁻¹ near 1 AU (Gopalswamy et al. 2000; Schwenn et al. 2005; Richardson & Cane 2010), also clearly underlines the influence of aerodynamic drag experienced by CMEs in the IP medium (Cargill 2004). Each CME has different initial characteristics, viz., initial speed, expansion speed, mass, angular width, density, and magnetic field, and is ejected in different solar wind conditions. These effects, when coupled together, decide the dynamics of CMEs in the IP medium. Therefore, the estimation of the CME arrival time using any prediction model, with a true speed estimated from the 3D reconstruction method using coronagraph (COR2) data as the only input, may not be accurate. A recent statistical study of CME kinematics based on the estimation of the 3D speed using forward modeling (Thernisien et al. 2009) and implementing the Gopalswamy et al. (2000) empirical model has reported an average error of nearly 10 hr between the observed and predicted travel times (Kilpua et al. 2012).

Our present study of eight CMEs attempts to understand the 3D propagation of CMEs by tracking them continuously throughout the IP medium. For this purpose, we have used the geometric triangulation (referred to as GT, hereafter) technique developed by Liu et al. (2010) on the time–elongation maps (Sheeley et al. 1999), popularly known as *J*-maps, constructed from COR2 and HI observations. Based on the GT using coronagraph (COR2) and HI images, the true kinematics of a CME can be estimated. These estimated values are used as inputs in the drag-based model (Vršnak et al. 2013) beyond the distance where a CME could not be tracked unambiguously, and its arrival time as well as its transit velocity at the L1 point are predicted. The predicted arrival time and transit velocity of the CME at L1 are then compared with the actual arrival time and transit velocity as observed by in situ instruments, e.g., ACE and WIND. The predicted arrival time is also compared with the arrival time estimated using the true speed obtained by the tie-pointing procedure (scc_ measure: Thompson 2009) from SECCHI/COR2 data alone.

In Section 2, we describe observations analyzed in this paper and the implementation of 3D reconstruction techniques. Application of these techniques on eight CMEs is presented in Section 3. The obtained results and discussions are presented in Section 4 and a summary appears in Section 5. Our study reveals the importance of heliospheric imaging and the GT technique on *J*-maps to improve the prediction of the arrival time and transit velocity at L1 (near 1 AU) as well as the direction of propagation of CMEs in the IP medium.

2. OBSERVATIONS AND ANALYSIS TECHNIQUES

Since its launch in 2006, the twin *STEREO* spacecraft (*STEREO A* and *B*) have enabled the 3D imaging of a CME from its birth in the corona to 1 AU and beyond. *STEREO A* moves faster and is slightly closer to the Sun than the Earth and leads the Earth in its orbit while *STEREO B* is a little farther from the Sun and trails the Earth. The separation between the two spacecraft increases by about 45° yr⁻¹. Both spacecraft have an identical imaging suite package called SECCHI. *STEREO*/SECCHI is a suite of five telescopes (Extreme Ultraviolet Imager

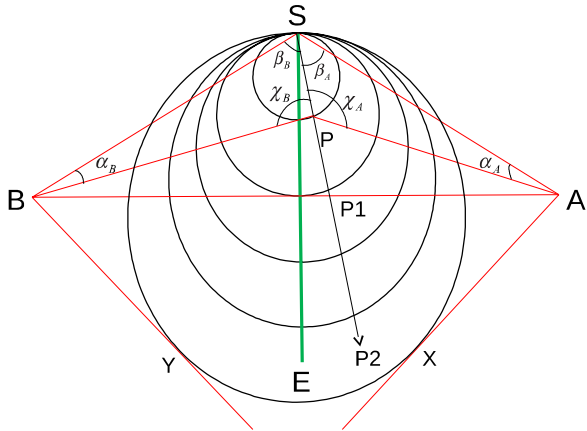


Figure 1. Schematic diagram of geometric triangulation for a moving feature between the two spacecraft *STEREO A* and *B*, in the direction of the arrow. Line SE represents the Sun–Earth line and α , β , and χ denote the elongation, propagation, and scattering angles, respectively. Subscripts *A* and *B* represent angles measured from the *STEREO A* and *B* view points.

(A color version of this figure is available in the online journal.)

(EUVI): $1\text{--}1.7 R_{\odot}$; COR1: $1.5\text{--}4.0 R_{\odot}$; COR2: $2.5\text{--}15.0 R_{\odot}$; HI1: $15\text{--}90 R_{\odot}$; and HI2: $70\text{--}330 R_{\odot}$) that image the CMEs continuously from the Sun to the Earth and beyond. Both coronagraphs (COR1 and COR2) are pointed on the Sun while both HIs (HI1 and HI2) are off-pointed from the Sun at a solar elongation of 14° and 53.7° , respectively (Eyles et al. 2009). HI1 and HI2 have a wide FOV of 20° and 70° , respectively, and have their optical axes aligned in the ecliptic plane. With these imaging instruments, a CME can be observed with a solar elongation ranging from 0.4° to 88.7° .

We carried out the tie-pointing procedure of 3D reconstruction (Thompson 2009), which is based on the epipolar geometry (Inhester 2006), to estimate the 3D kinematics of CMEs in the COR2 FOV. We estimated the true kinematics of all eight CMEs selected for our study by implementing this technique on SECCHI/COR2 images.

In order to understand the propagation of CMEs in the IP medium, we used the GT technique developed by Liu et al. (2010), which assumes that the same feature of a CME is observed from two different view points and that the difference in measured elongation angles (angle of the feature with respect to the Sun–spacecraft line) for the tracked feature from *STEREO A* and *B* is entirely due to two viewing directions. Using imaging observations and a Sun-centered coordinate system, the elongation angle of a moving feature can be calculated. The details of the GT technique in an ecliptic plane applicable for a feature propagating between the two spacecraft have been explained in Liu et al. (2010). To estimate the propagation direction and radial distance of CME features, Equations (1)–(4) of Liu et al. (2010) are used in our study.

A schematic diagram for the location of the twin spacecraft and the tracked feature is shown in Figure 1. Liu et al. (2010) did not take into account the effects of Thomson scattering and the geometry of CMEs. In principle, the Thomson scattering physics and geometry of CMEs need to be considered. The total scattered intensity received by an observer at a certain location depends on the radial and tangential component of the scattered radiation from the scattering source (Howard & Tappin 2009a). The tangential component of the scattered radiation does not depend on the scattering angle but the radial component does. However, in our selection of events, where a CME is

moving nearly toward the Sun–Earth line, both view directions (line-of-sight AP and BP as shown in Figure 1) will be nearly symmetrically located from the Sun–Earth line. Therefore, the scattering angles (χ_A and χ_B) for both the observers will only be slightly different and the resulting difference in the received radial intensity for both the observers (*STEREO A* and *B*) will be small. The approximation that both observers view the same part of CME may not be true when Earth-directed CMEs are at a large distance from the Sun (for view directions AX and BY as shown in Figure 1) and also near the Sun for very wide or rapidly expanding CMEs. It is also rather unlikely that the same feature of a CME will be tracked in each successive image, even from one observation point. Therefore, it seems reasonable to take the geometry of the CME into account. But idealistic assumptions made about geometry can result in new errors in the estimated kinematics.

In the present study, we reconstruct the CMEs using a straightforward and easy procedure of GT on HI observations to relate remote sensing observations with in situ observations for a practical application to the space weather prediction scheme. We exclude the geometry and complex treatment of Thomson scattering physics. Optimistically, taking into account the aforementioned points, we briefly note that errors arising from implementing the GT technique, even after neglecting many real effects, will be minimized particularly for Earth-directed CME events.

3. SELECTED EVENTS

In the present study, we have selected eight Earth-directed CMEs observed on different dates after the launch of the *STEREO* spacecraft. All these CMEs have been observed by the twin *STEREO* spacecraft with different separation angles between them. These CMEs have been observed from their birth in the corona through the inner heliosphere by coronagraphs and HIs, respectively. These selected CMEs were observed on 2008 December 12, 2010 February 7, 2010 February 12, 2010 March 14, 2010 April 3, 2010 April 8, 2010 October 10, and 2010 October 26. These CMEs were also observed by in situ instruments. Remote sensing observational data of CMEs by the twin *STEREO* spacecraft are taken from UKSSDC (<http://www.ukssdc.ac.uk/solar/stereo/data.html>). In situ observations of CMEs were obtained from the *ACE* and *WIND* spacecraft situated at the L1 point, upstream from the Earth. We used the OMNI data with 1 minute time resolution for solar wind parameters, e.g., magnetic field, proton velocity, proton density, proton temperature, and plasma beta. We also used the latitude and longitude of magnetic field vector data with a time resolution of 1 hr. Combined OMNI data were taken from NASA CDAWeb (<http://cdaweb.gsfc.nasa.gov>). We present our analysis for each event sequentially; the event of 2008 December 12 has been described with significant depth to explain the implemented techniques. Analysis for the other events has been carried out by adopting exactly the same methodology as explained for the event of 2008 December 12 and is summarized only briefly.

3.1. 2008 December 12 CME

3.1.1. Remote Sensing Observations

This CME was observed in SECCHI/COR1 Ahead at 04:35 UT in the NE quadrant and in SECCHI/COR1 Behind at 04:55 UT in the NW quadrant. *SOHO/LASCO* observed this as a partial halo CME having an angular width of 184° with

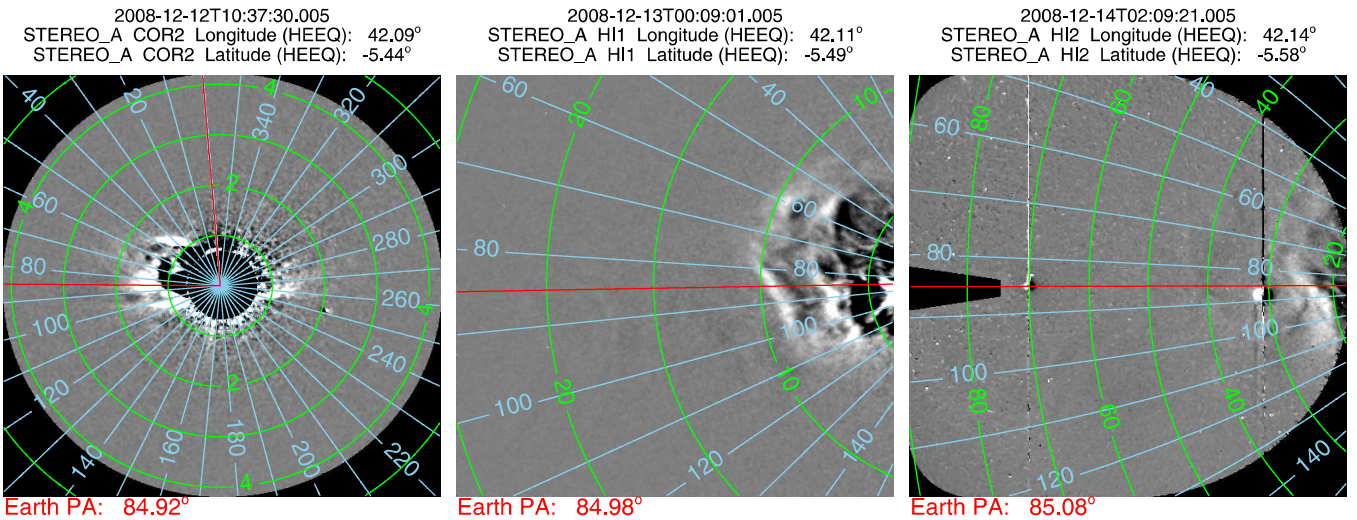


Figure 2. Left, middle, and right panels show the running difference image taken by COR2, HI1, and HI2, respectively, on *STEREO/SECCHI* Ahead with contours of the elongation angle (green) and the position angle (blue) overlaid. The horizontal red line is along the ecliptic at the position angle of the Earth. The vertical red line in the left panel marks the zero degree position angle.

(A color version of this figure is available in the online journal.)

a linear speed of 203 km s^{-1} (online LASCO CME catalog: http://cdaw.gsfc.nasa.gov/CME_list/; see Yashiro et al. 2004). *SOHO/LASCO* could follow this CME out to $12 R_\odot$ where its quadratic speed was 322 km s^{-1} . The *SOHO/LASCO* catalog reported this accelerating CME as a poor event. The CME was associated with a filament eruption that started at 03:00 UT in the northeast quadrant observed in SECCHI/EUVI Ahead (A) 304 Å images. The appearance of the CME in the SECCHI Ahead COR2, HI1, and HI2 data is displayed in Figure 2.

STEREO/HI detects photospheric light scattered from free electrons in K-corona and IP dust around the Sun (F-corona) similar to a coronagraph (Billings 1966; Tappin 1987; Vourlidas & Howard 2006; Howard & Tappin 2009b). It also detects the light from the stars and planets within its FOV. The F-corona is stable on a timescale far longer than the nominal image cadence of 40 and 120 minutes for the HI1 and HI2 cameras, respectively. It has been often observed that when CMEs leave the coronagraphic FOV and enter the HI FOV, the Thomson-scattered signal is too low to identify a particular feature in both sets of images obtained by *STEREO A* and *B*. Therefore, for tracking a CME in the IP medium, the method of the time–elongation map (*J*-map) is used, which was initially developed by Sheeley et al. (1999) for LASCO images. Rouillard et al. (2009) implemented the same technique on HI data to reveal the outward motion of plasma blobs in the IP medium. A running difference technique (Sheeley et al. 1997), in which each image is presented after the subtraction of the previous image, gives an image with a dominant K-corona contribution. By taking an image difference, the changes in electron density between consecutive images are highlighted and density enhancements and depletions are revealed.

We constructed the *J*-maps along the ecliptic plane using long-term background-subtracted running difference images from COR2, HI1, and HI2 taken by the *STEREO A* and *B* spacecraft. Prior to this, the HI image pair was aligned to remove the stellar contribution from the difference images; this technique requires precise pointing information of the HI instrument (Davies et al. 2009). For this purpose, we used the level 2 HI data that were corrected for cosmic rays, shutterless

readout, saturation effects, flat fields, and instrument offsets from spacecraft pointing. Also, the long-term background was subtracted from these images. For the coronagraph data, we used the level 0 data and processed these before taking the running difference. We calculated the elongation and position angles for each pixel of the difference images and extracted a strip of constant position angle interval along the position angle of the Earth for COR2, HI1, and HI2 images. The position angle tolerance considered for the COR2 is 5° and 2.5° for both HI1 and HI2. We binned the pixel of the extracted strip over a specific elongation angle bin size, viz., $0:01$ for COR2 and $0:075$ for both HI1 and HI2. Furthermore, we took the resistant mean for each bin to represent the intensity at a corresponding elongation angle. The resistant mean for each elongation bin was scaled to reveal a significant elongation bin. These scaled resistant means were stacked as a function of time and elongation to produce what is known as a time–elongation map (*J*-map). This map is shown in Figure 3 for the CME of 2008 December 12. In this *J*-map, the bright curve with positive inclination reveals the evolution of the CME. In the *J*-map constructed from images taken by the *STEREO A* spacecraft, there are two nearly horizontal lines in the HI2 FOV that start at an elongation angle of $30:7$ and $70:1$, respectively. These lines are due to the appearance of the planets Venus and Earth, respectively, in the HI2 A FOV. In the HI2 A images taken on 2008 December 12 at 00:09:21 UT, Venus is seen at a position angle (helioprojective radial longitude) of $88:1$ and an elongation angle (helioprojective radial latitude) of $30:7$. These measurements correspond to the pixels 830×487 in the image of 1024×1024 size. At this time, the Earth is observed corresponding to pixels 277×509 in the HI2 A image and to pixels 655×510 in the HI2 B image. The appearance of planets in the HI FOV saturates the pixels where they are found and also their signal bleeds up and down in the CCD, creating vertical columns of saturated pixels in the HI images (Figure 2). In the *J*-map constructed from the *STEREO B* images, one horizontal line is observed that starts at an elongation angle of $63:9$ and is due to the appearance of planet Earth in the HI2 B FOV. Vertical columns of saturated pixels correspondingly appear in the HI2 B images.

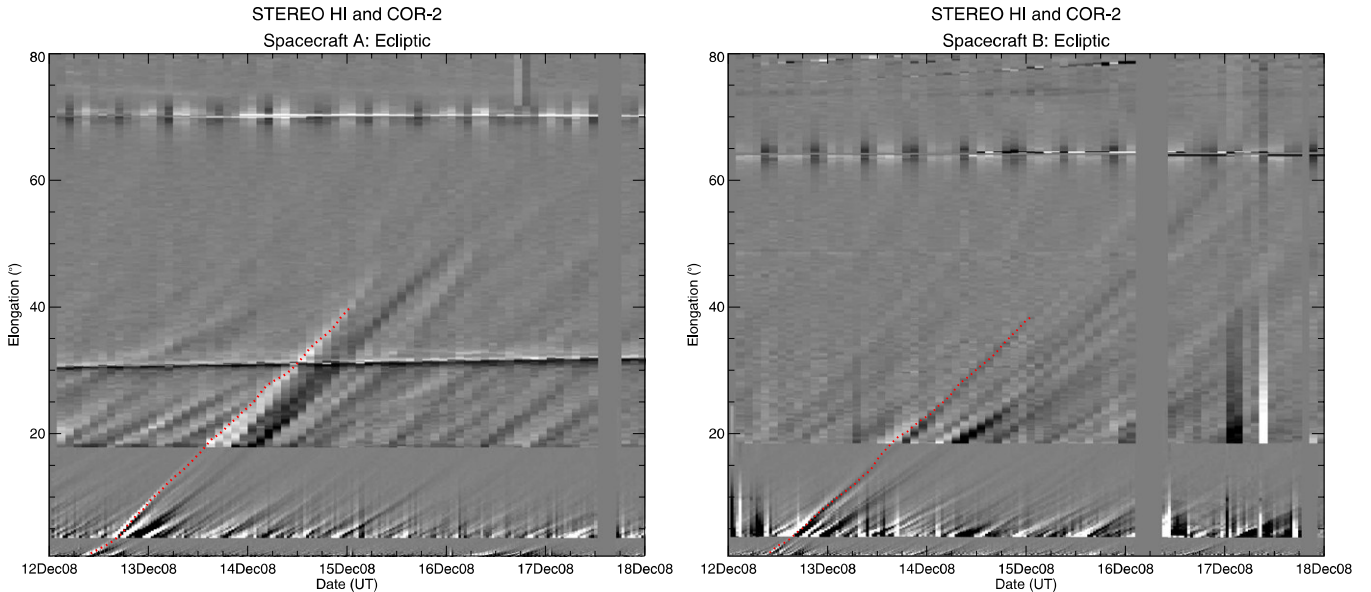


Figure 3. Time–elongation map (J -map) for *STEREO A* (left) and *STEREO B* (right) for the interval of 2008 December 12–18. The red dot shows the tracked feature corresponding to the 2008 December 12 CME. The tracked dot is over plotted on the J -map to mark the elongation variation with time.
(A color version of this figure is available in the online journal.)

By tracking a CME continuously in the J -maps, separately for the *STEREO A* and *B* images, independent elongation angles of a moving CME feature are estimated. Using precise separation angle between *STEREO A* and *B*, their heliocentric distances, and elongation angles as inputs in the GT technique (Liu et al. 2010), we obtain the distance and propagation direction of the moving CME feature. Its velocity is calculated from the estimated distance profile by using numerical differentiation with a three-point Lagrange interpolation method. Figure 4 shows the kinematics of the CME of 2008 December 12. Red vertical lines show the error bars that are mathematically calculated, taking into account the uncertainty in the measurements of the elongation angles. We have considered an uncertainty of 5 pixels in measurements of elongation angles, which is equivalent to uncertainties of $0^\circ.02$, $0^\circ.1$, and $0^\circ.35$ in elongation for the COR2, HI1, and HI2 images, respectively.

To estimate the true kinematics of the 2008 December 12 CME in the COR2 ($2.5\text{--}15 R_\odot$) FOV, we carried out 3D reconstruction of its selected features. For this, we used SECCHI/COR2 images. After calibration and background subtraction, we applied the tie-pointing method (scc_measure: Thompson 2009) on both sets of images taken by COR2 A and B. On the identification of a feature along the leading edge observed in both sets of images, we found a correspondence between pixels of both images. The lines of sight corresponding to those pixels were found and tracked backward; we obtained a point of intersection, which is the true 3D coordinate of the selected feature (Inhester 2006). The kinematics obtained after 3D reconstruction using COR2 data is shown in Figure 5. The true Stonyhurst heliographic latitude and longitude have been plotted in Figure 5, which shows that the CME was Earth directed.

3.1.2. Estimation of the Arrival Time and Transit Speed at L1

Using the GT method on HI data, we have estimated the kinematics of the CME of 2008 December 12 out to approximately $138 R_\odot$. We assume that after traversing such a large distance, the speed of the CME will depend solely on aerodynamic drag. Therefore, we can use the quadratic form of the drag acceler-

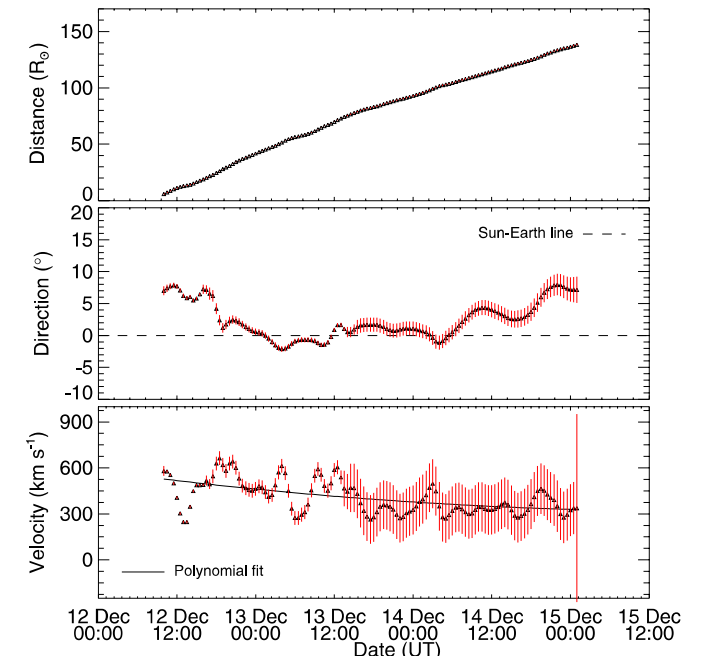


Figure 4. From top to bottom, panels show the distance, propagation direction, and velocity, respectively, of the 2008 December 12 CME. In the second panel, the horizontal dashed line represents the Sun–Earth line. The red vertical lines show the error bars. In the bottom panel, velocity is estimated from adjacent distances using three-point Lagrange interpolation; error bars are accordingly large. The solid line in the third panel is the polynomial fit to the actual velocity data points.
(A color version of this figure is available in the online journal.)

ation $a = -\gamma(v - w)|v - w|$, where v is the instantaneous CME speed and w is the ambient solar wind speed (Cargill 2004 and references therein). The drag parameter is expressed as $\gamma = (c_d A \rho_w / M + M_v)$, where c_d is the dimensionless drag coefficient, A is the cross-sectional area of CME perpendicular to its direction of propagation, ρ_w is the ambient solar wind density,

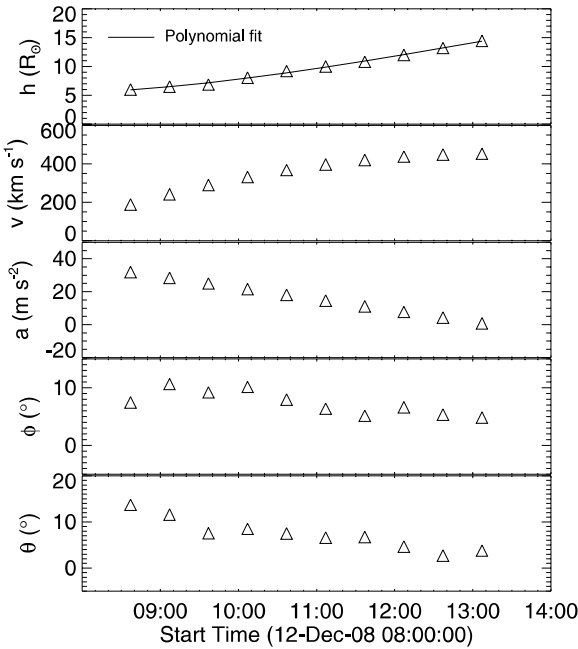


Figure 5. From top to bottom, the panels show the estimated true height, radial velocity, acceleration, longitude and latitude, and time on the X-axis using the tie-pointing method. Velocity and acceleration are calculated by first- and second-order differentiation, respectively, by fitting a third-order polynomial to the true height data.

M is the mass of CME, and M_v is the virtual mass that is written as $M_v = \rho_w V/2$, where V is the volume of CME.

We used the DBM developed by Vršnak et al. (2013) to estimate the arrival time of the 2008 December 12 CME. In the DBM, it is assumed that after $20 R_\odot$, the drag parameter and ambient solar wind speed do not change with heliocentric distance. The DBM also assumes that $A \propto r^2$, $\rho_w \propto r^{-2}$, $M = \text{constant}$, and $c_d = \text{constant}$, which are valid after traversing a long distance. Moreover, the virtual mass M_v is assumed to be negligibly small. A continuity equation for an isotropic flow added with $\rho_w \propto r^{-2}$ gives $w = \text{constant}$. By estimating the mass of the CME and considering it to be constant beyond a distance of $20 R_\odot$, a solar wind density from Leblanc et al. (1998), a volume using the cone model of a CME (Xie et al. 2004), and the drag parameter can be calculated at any heliocentric distance. However, the statistical analysis of Vršnak et al. (2013) for a sample of events shows that the drag parameter lies in the range 0.2×10^{-7} – $2.0 \times 10^{-7} \text{ km}^{-1}$. Their statistical analysis shows that the ambient solar wind speed should be chosen to lie between 300 and 400 km s⁻¹ for a slow solar wind environment. However, if there is a coronal hole in the vicinity of the source region of the CME, the solar wind speed value should be chosen to be between 500 and 600 km s⁻¹. Since there is limited accuracy and difficulty in reliably estimating variables on which the drag parameter depends (mass, cone angle of the CME, and solar wind density), we used the extreme values of the range of the drag parameter for CMEs in our study. The limitation on the accurate and reliable estimation of the CME mass using single coronagraph images has been discussed in Vourlidas et al. (2000). Colaninno & Vourlidas (2009) discussed limitations using multiple view points (SECCHI/COR). Choosing extreme values of the range of the drag parameter, we estimate the maximum possible errors that can occur due to CMEs having different characteristics.

We used the estimated kinematics as inputs for three different approaches in order to predict the arrival time of CMEs at L1 ($\approx 1 \text{ AU}$). These three approaches are described as follows.

1. *From DBM with inputs from GT on COR2 and HI.* We used the DBM, combined with the inputs obtained by implementing the GT technique on COR2 and HI observations. For the inputs in the DBM, we used the initial radial distance and CME take-off date and time are obtained from the last data points estimated in the GT scheme. The initial take-off velocity is taken as the average of the last few velocity points of the fitted polynomial for the estimated velocity in the ecliptic plane. In this particular event of 2008 December 12, we used the DBM with a take-off date and time of 2008 December 15 at 01:00 UT, a take-off distance of $138.3 R_\odot$, a take-off velocity of 330 km s^{-1} , an ambient solar wind speed of 350 km s^{-1} , and a drag parameter of $0.2 \times 10^{-7} \text{ km}^{-1}$. Using these values, we obtained its arrival time as 20:25 UT on 2008 December 16 with a transit speed of 331 km s^{-1} at the L1 point. Using the maximum value of the average range of the drag parameter ($2 \times 10^{-7} \text{ km}^{-1}$) and keeping other parameters the same in the DBM, the predicted arrival time of the CME was found to be 19:55 UT on 2008 December 16 with a transit speed of 338 km s^{-1} .
2. *Using a polynomial fit of distance estimated from the GT technique with COR2 and HI data.* The radial distance of a moving feature, which is estimated by implementing the GT technique, is fitted to a second-order polynomial. By extrapolation we obtained the arrival time of the CME at L1. The predicted arrival time is 06:23 UT on 2008 December 17. In an earlier study by Liu et al. (2010), the predicted arrival time for this CME was found to be 16:00–18:00 UT on 2008 December 16. These authors extrapolated the estimated distances. The difference in the arrival times may arise due to different extrapolation techniques but is most likely due to tracking of different features in J -maps. It highlights the possible error in the arrival time prediction due to manual tracking of ambiguous edges of bright features in the J -maps. Since fitting the estimated distance using a second-order polynomial includes all the points with different velocity phases, this technique may result in greater uncertainties in the extrapolated arrival times.
3. *Using true speed estimated in the COR2 FOV.* From the 3D reconstruction of the CME leading edge using the tie-pointing (scc_measure) method on SECCHI/COR2 data, the true velocity was found to be 453 km s^{-1} at $14.4 R_\odot$ at 13:07 UT on 2008 December 12. With a simple assumption that the speed of a CME is constant beyond the COR2 FOV, the predicted arrival time at L1 is 01:45 UT on 2008 December 16.

An in-depth analysis of this CME was carried out earlier by several researchers using *STEREO* COR and HI observations. Byrne et al. (2010) predicted the arrival time of this CME using 3D reconstruction of the CME front and the ENLIL simulation. They found that the predicted arrival time of the CME agreed well with the CME front plasma pileup ahead of a magnetic cloud observed in situ by the ACE and WIND spacecraft. In the study of Davis et al. (2009), three different features within the CME were tracked in the heliosphere from an independent location of the *STEREO* spacecraft and their speed, direction, and arrival time at the L1 point were estimated.

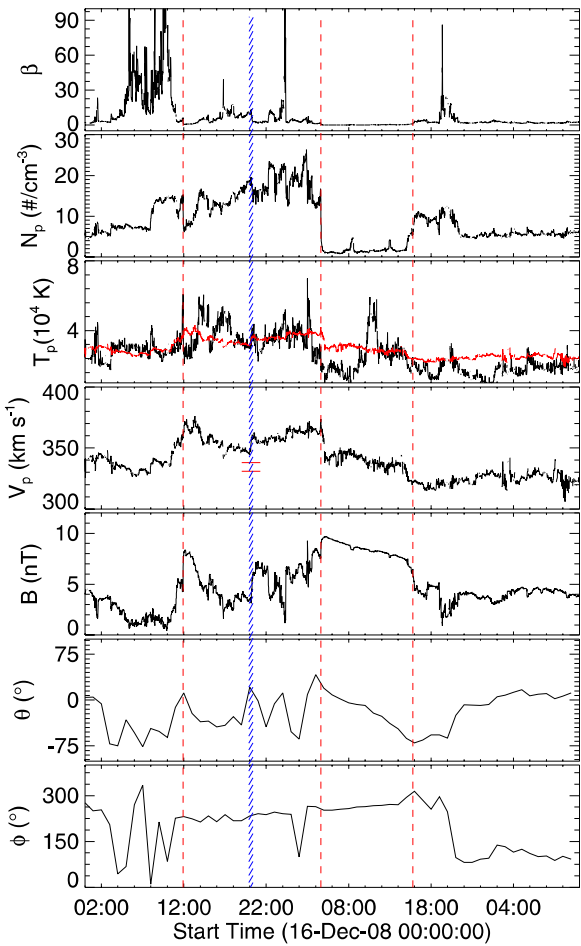


Figure 6. From top to bottom, panels show the variation of plasma beta, proton density, proton temperature, proton velocity, magnitude of magnetic field, and latitude and longitude of the magnetic field vector, respectively, corresponding to the CME of 2008 December 12. From the left, the first, second, and third vertical dashed lines (red) mark the arrival time of the CME sheath and the leading and trailing edges of a magnetic cloud, respectively. The hatched region (blue) marks the interval of the predicted arrival time of the tracked feature. In the third panel from the top, the expected proton temperature is shown as a red curve and in the fourth panel horizontal lines (red) mark the predicted velocities at L1.

(A color version of this figure is available in the online journal.)

3.1.3. *In situ Measurements of the CME*

Near the Earth, CMEs can be identified by a combination of various signatures observed in situ (Zurbuchen & Richardson 2006). Figure 6 shows the predicted arrival time and transit velocity at in situ spacecraft situated at the L1 point. These values correspond to extreme values of the average range of the drag parameter used in DBM, as discussed in the previous section. The first dashed vertical line (red) marks the arrival of the sheath at 11:55 UT on December 16 and the second dashed vertical line (red) marks the arrival of the leading edge of a magnetic cloud (Klein & Burlaga 1982) at 04:39 UT on December 17. The third dashed vertical line (red) marks the trailing edge of a magnetic cloud at 15:48 UT on 2008 December 17. The hatched region (blue) shows the predicted arrival time (with uncertainties due to the range of values of the drag parameter adopted in DBM) using the DBM. In the fourth panel, two red horizontal lines mark the predicted transit velocities at L1 of the tracked feature corresponding to different values of the drag parameter used in the DBM. In the third

panel (from the top), the red curve shows the expected proton temperature calculated from the observed in situ proton speed (Lopez & Freeman 1986; Lopez 1987).

3.2. 2010 February 7 CME

SOHO/LASCO observed this CME on 2010 February 7 at 03:54 UT as a halo CME with a linear speed of 421 km s^{-1} . The speed of the CME was nearly constant in the LASCO FOV. It appeared in the COR1 FOV of *STEREO A* and *B* at east and west limbs, respectively, at 02:45 UT. We constructed the *J*-map for this CME as described for the 2008 December 12 CME (Section 3.1.1). At the time of this CME, the distances of *STEREO A* and *B* from the Sun were 0.96 and 1.01 AU, respectively, and the separation angle between them was $135^\circ.6$. In the HI2 A and HI2 B FOVs, planets Earth and Mars were visible. As a result, a vertical column of saturated pixels in the images appears and parallel lines in the *J*-maps corresponding to the planets' elongation angles are visible. This event was tracked in the heliosphere and an independent elongation of a moving feature of the CME from two vantage points was estimated using the *J*-maps. These estimated independent elongation angles and the positional inputs of the twin *STEREO* spacecraft were used in the GT scheme to estimate the kinematics of the CME. The obtained kinematics are shown in Figure 7, in which the gap in the estimated parameters is due to the existence of a singularity in the GT scheme. The estimated points in this range have non-physical variations; these have therefore been removed (Liu et al. 2011). We found that the singularity in the GT scheme occurs when the sum of both independent elongation angles measured from two spacecraft and the separation angle between two spacecraft becomes nearly 180° . In this situation, the line of sight from the two view points of the spacecraft coincides along their entire length. Therefore, a single value of longitude cannot be obtained in this scenario. In Figure 1, we show that the line of sight from the two locations of *STEREO A* and *B* (AP1 and BP1) will be parallel for point P1 to be triangulated. Therefore, in this case, a singularity will occur in a triangulation scheme. As the *STEREO* mission progressed, the separation angle between the two spacecraft increased. Therefore the occurrence of a singularity will be an issue at smaller elongation angles.

We used the drag model with inputs from the last data point of estimated kinematics to calculate the arrival time of the CME at the L1 point. Using a take-off distance of $171 R_\odot$, a take-off time of 2010 February 10 at 03:30 UT, a take-off velocity of 455 km s^{-1} , a drag parameter of $0.2 \times 10^{-7} \text{ km}^{-1}$, and an ambient solar wind speed of 350 km s^{-1} , we obtained a predicted arrival time of 21:40 UT on February 10 and a transit speed 442 km s^{-1} at the L1 point. Keeping all the input parameters the same but changing the drag parameter to $2.0 \times 10^{-7} \text{ km}^{-1}$, the predicted arrival time is 22:50 UT on February 10 and the transit speed is 393 km s^{-1} . Using a second-order polynomial fit for the estimated distance points and extrapolating it, we obtained an arrival time of 00:50 UT on February 11 at the L1 point. We also carried out the 3D reconstruction of this CME using SECCHI/COR2 data and estimated the true heliographic coordinates of a selected feature along the leading edge. The true velocity was estimated as 480 km s^{-1} at $13.5 R_\odot$ at 06:39 UT on 2010 February 7. Assuming that the true velocity of the CME is constant beyond the COR2 FOV, the predicted arrival time is 14:55 UT on 2010 February 10 at L1.

The in situ observations of this CME are shown in Figure 8. The first vertical dashed line (red) at 01:00 UT on February 11 marks the arrival of a weak shock or CME sheath, the second

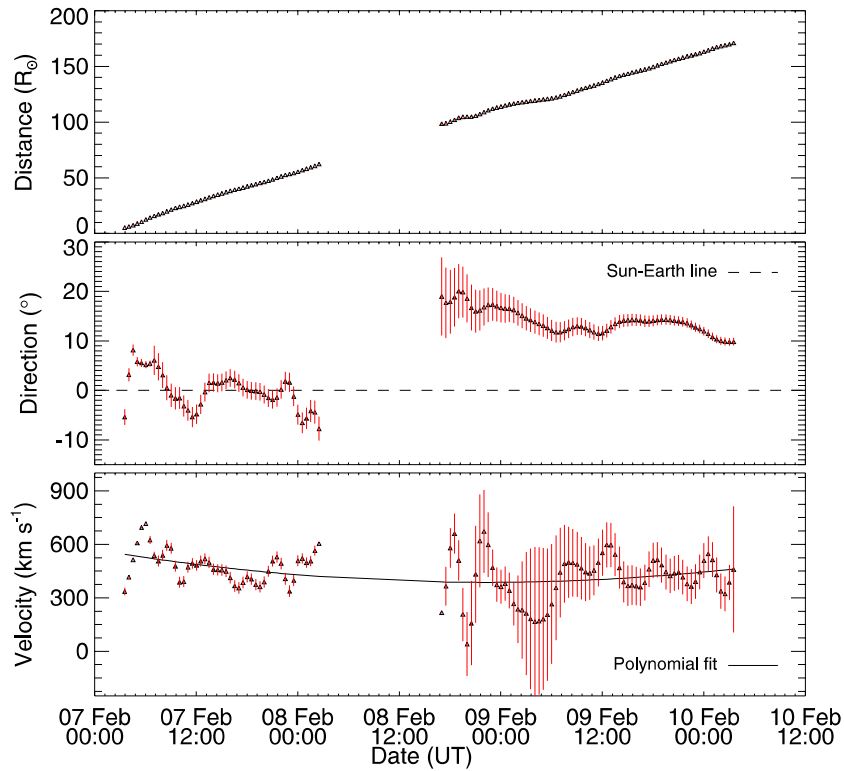


Figure 7. From top to bottom, panels show the distance, propagation direction, and velocity, respectively, of the 2010 February 7 event. The details are given in the caption to Figure 4.

(A color version of this figure is available in the online journal.)

vertical dashed line (red) at 12:47 UT marks the arrival of the CME leading edge, and the third vertical dashed line (red) at 23:13 UT marks the trailing edge of the CME. The hatched region (blue) shows the predicted arrival time with uncertainties due to extreme values of the drag parameter with the same inputs from the estimated kinematics employed in the DBM.

3.3. 2010 February 12 CME

This CME was observed in the NE quadrant in SECCHI/COR1 A observations and in the NW quadrant in SECCHI/COR1 B images at 11:50 UT on February 12. It was also observed by *SOHO/LASCO* at 13:42 UT as a halo CME with a linear speed of 509 km s^{-1} . It was observed to decelerate in the LASCO FOV and its speed at final height ($\approx 25 R_\odot$) was measured to be 358 km s^{-1} . We constructed the *J*-maps using COR2, HI1, and HI2 observations for the CME. In the SECCHI/HI2 A & B FOV, planets Earth and Mars were visible as parallel lines corresponding to their elongation angles in the *J*-maps. The independent elongation angle of a moving feature from two view points was estimated by tracking the bright, positively inclined feature in the *J*-maps corresponding to this CME. Implementing the GT technique, the kinematics of the CME were estimated and are shown in Figure 9. The data gap in this plot is due to the occurrence of a singularity in the GT scheme; details are explained in Section 3.2.

To predict the arrival time of this CME, we combined the estimated kinematics with the DBM. Input parameters used in the DBM were calculated in the same way as explained earlier in Section 3.1.2. Using the inputs, e.g., an initial take-off distance of $183 R_\odot$, a take-off time of 2010 February 15 at 01:44, a take-off velocity of $\sim 450 \text{ km s}^{-1}$, an ambient solar wind speed of 350 km s^{-1} , and a drag parameter of $0.2 \times 10^{-7} \text{ km}^{-1}$ in

the DBM, the predicted arrival time and transit speed of the CME at L1 are 14:35 UT on 2010 February 15 and 442 km s^{-1} , respectively. If the drag parameter is taken as $2.0 \times 10^{-7} \text{ km}^{-1}$ in the DBM, keeping the rest of the input parameters same, the predicted arrival time of the CME is found to be 15:20 UT on 2010 February 15 and the transit speed is found to be 401 km s^{-1} .

The identification of the CME near the Earth is studied by analyzing the in situ data (Figure 10). In this figure, the first vertical dashed line (red) at 18:42 UT on February 15 marks the arrival of shock, the second dashed vertical line (red) at 04:32 UT on February 16 marks the arrival of the CME leading edge, and the third vertical dashed line (red) at 12:38 UT on February 16 marks the CME trailing edge. The hatched region with blue color marks the predicted arrival time (with uncertainties due to extreme values of the drag parameter used in the DBM) using estimated kinematics parameters combined with the DBM. Using the second-order polynomial fit for distance, we obtained the predicted arrival time of CME at L1 as 16:07 UT on February 15. Furthermore, from 3D reconstruction in the COR2 FOV, the true velocity of the leading edge of CME was estimated to be 867 km s^{-1} at a distance of $14.8 R_\odot$ at 14:54 UT on February 12. Considering that the CME speed was constant up to L1, the predicted arrival time at L1 is 11:02 UT on February 14.

3.4. 2010 March 14 CME

This CME was observed on 2010 March 14 by SECCHI/COR1 A in the NE quadrant and by SECCHI/COR1 B in the NW quadrant of the coronagraphic images. *SOHO/LASCO* observed this as a partial halo (angular width $\approx 260^\circ$) CME at 00:30 UT on March 14 with a linear speed of 351 km s^{-1} . In the LASCO FOV, a nearly constant speed of the CME was observed. In the *J*-maps constructed from COR and HI A images, this

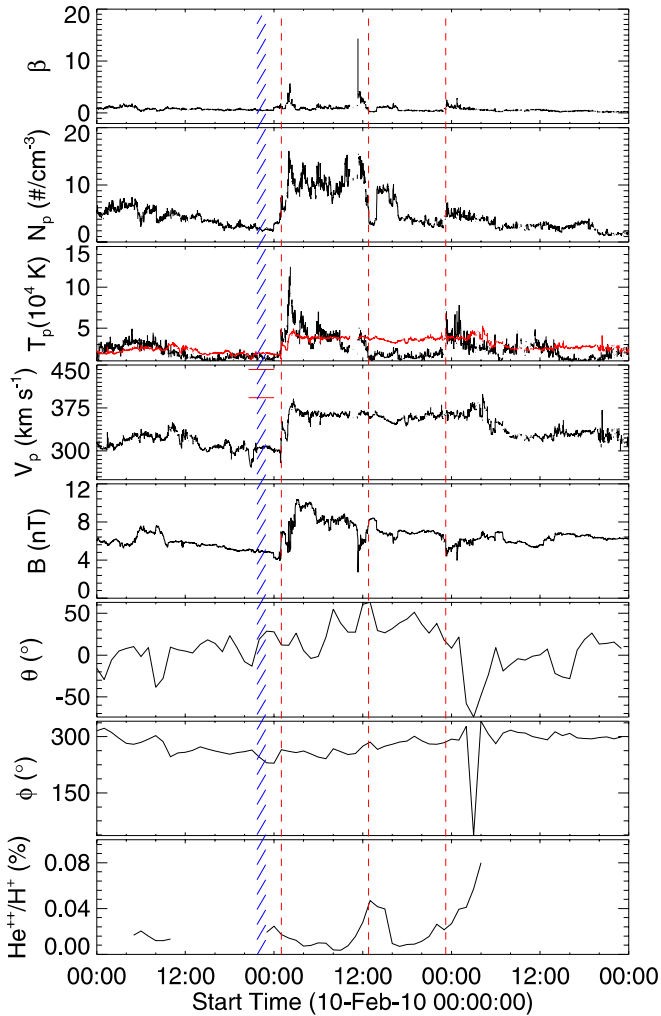


Figure 8. From top to bottom, panels show the plasma beta, proton density, proton temperature, proton velocity, magnitude of magnetic field, latitude and longitude of the magnetic field vector, and the alpha to proton ratio, respectively, corresponding to the CME of 2010 February 7. From the left, the first, second, and third vertical dashed lines (red) mark the arrival time of the sheath and the leading and trailing edges of the CME, respectively. The hatched region (blue) shows the interval of the predicted arrival time of the tracked feature. In the third panel from the top, the expected proton temperature is shown as a red curve and in the fourth panel two horizontal lines (red) mark the predicted velocities of the tracked feature at L1.

(A color version of this figure is available in the online journal.)

CME could be tracked nearly up to 35° while in the J -maps constructed from COR and HI B images, tracking was possible up to 50° . In the SECCHI/HI2 A FOV, planets Earth and Mars were seen while in the HI2 B FOV only the Earth could be seen. We tracked the CME in the heliosphere and estimated its independent elongation from two *STEREO* locations. These elongation angles and the separation angle between the twin *STEREO* spacecraft were used as inputs in the GT scheme to obtain the propagation direction and the distance of the CME. Velocity was calculated from the adjacent distances using three-point Lagrange interpolation. The kinematics of this CME are shown in Figure 11. The occurrence of singularity has been also noticed for this case in the GT scheme. Therefore, the estimated kinematics in the time range of the singularity are not shown.

The estimated kinematics are used as inputs in the DBM to predict the arrival time of the CME at the L1 point. We used the

DBM with a take-off distance of $135.9 R_\odot$, a take-off velocity of 460 km s^{-1} , a take-off date and time of 2010 March 16 at 12:07 UT, an ambient solar wind speed of 350 km s^{-1} , and a drag parameter of $0.2 \times 10^{-7} \text{ km}^{-1}$ as inputs and obtained its predicted arrival time at 21:10 UT on March 17 with a transit velocity 437 km s^{-1} at L1. Keeping all these input parameters the same and using the maximum value of the statistical range of the drag parameter ($2 \times 10^{-7} \text{ km}^{-1}$) in the DBM, we obtained a predicted arrival time of 01:00 UT on March 18 and a transit velocity of 378 km s^{-1} at L1. The predicted arrival time of the CME at L1, using the second-order polynomial fit for distance, is 16:21 UT on March 17. We also implemented the tie-pointing method of 3D reconstruction on the leading edge of the CME in the COR2 FOV and estimated the true kinematics of a CME feature. Assuming that the true speed (335 km s^{-1}) estimated at true height ($11 R_\odot$) at 03:54 UT on March 14 is constant beyond the COR2 FOV, the predicted arrival time of the CME is 00:17 UT on March 19.

The in situ observations for this CME are shown in Figure 12. In this figure, the first vertical dashed line (red) at 21:19 UT on March 17 marks the arrival of the CME leading edge and the second vertical dashed line (red) at 11:26 UT on March 18 marks the CME trailing edge. The hatched region (blue) shows the predicted arrival time of CME with range of uncertainty due to extreme values of the range of the drag parameter employed in the DBM.

3.5. 2010 April 3 CME

This CME was detected by *SOHO/LASCO* on 2010 April 3 at 10:33 UT as a halo. It had a projected plane-of-sky linear speed of around 668 km s^{-1} as measured from the LASCO images. It was observed at 09:05 UT by SECCHI/COR1 A in the SE quadrant and by SECCHI/COR1 B in the SW quadrant. The source region of the CME was NOAA AR 1059. The CME was accompanied by a filament disappearance, a post eruption arcade, coronal dimming, and EIT wave and a B7.4 long duration flare peaking at 09:54 UT (Liu et al. 2011).

We constructed the J -maps to track the CME in the heliosphere. Due to the appearance of the Milky Way Galaxy in the SECCHI/HI2 B images, the signal of this CME is not well pronounced. Therefore, it could not be tracked beyond 27° elongation in the J -map constructed from *STEREO B* images. Planets Earth and Mars are visible in the HI2 A images at 58.1° and 50.6° , respectively. The Earth is visible in the HI2 B images at 54.3° elongation. Independent elongation angles are extracted from the leading edge of the track of the CME in the J -maps. Then, the GT scheme is implemented to estimate the distance and propagation direction of the CME. The estimated kinematics are displayed in Figure 13; a data gap of approximately 6 hr in the estimated kinematics is due to the occurrence of a singularity in the implemented triangulation scheme.

We used the distance and velocity of the CME at the last estimated data point as inputs in the DBM to predict its arrival time at L1. At the time of this CME, the Earth was blown over by a high-speed solar wind stream emanating from the northern polar coronal hole. Due to the presence of this coronal hole and the generally large spatial scale of the CME, its kinematics will be partly governed by the high-speed stream as shown by Vršnak et al. (2013). They also showed that an ambient solar wind speed of 550 km s^{-1} and a low value of the drag parameter should be considered as inputs in the DBM. We used a CME take-off speed of 640 km s^{-1} , a take-off date and time of April 4 at 07:23 UT, a take-off distance of $100.8 R_\odot$, and a drag parameter

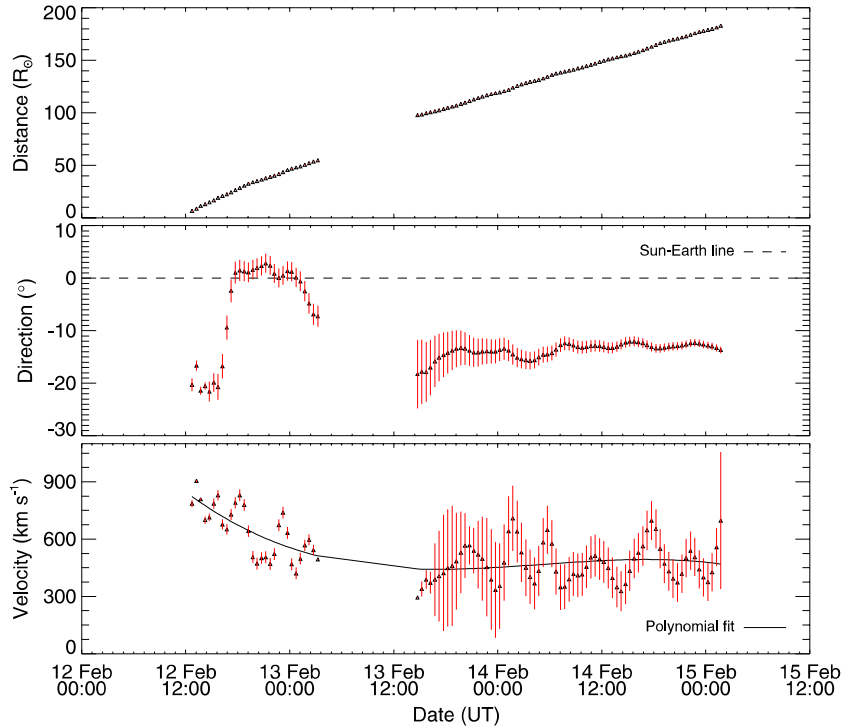


Figure 9. From top to bottom, panels show the distance, propagation direction, and velocity, respectively, of the 2010 February 12 event. For details see the caption to Figure 4.

(A color version of this figure is available in the online journal.)

of $0.2 \times 10^{-7} \text{ km}^{-1}$ in the DBM as inputs. We obtained the predicted arrival time of the CME at 17:35 UT on April 5 and a transit speed of 624 km s^{-1} at the L1 point. The predicted arrival time using extrapolation of the second-order polynomial fit of distance is obtained to be 09:00 UT on April 5. This CME has been studied in detail by Liu et al. (2011). They predicted the arrival by extrapolating the estimated distance at 12:00 UT on April 5, which is approximately the same as we predicted using a polynomial fit, with an error of 3 hr. We also carried out 3D reconstruction of the CME leading edge using SECCHI/COR2 data and obtained its true kinematics. Assuming that this true estimated velocity (816 km s^{-1}) at 12:24 UT on April 3 is constant beyond the COR2 FOV, the predicted arrival time of the CME at L1 is 11:25 UT on April 5.

We identified the CME in situ and the plot is shown in Figure 14. Here, the first vertical dashed line (red) marks the arrival of a shock at 8:28 UT on April 5, the second vertical dashed line (red) marks the arrival of the CME leading edge at 13:43 UT, and the fourth vertical dashed line (red) marks the CME trailing edge at 16:05 UT on April 6. The third vertical dashed line (blue) marks the predicted arrival time of the CME obtained after the estimated dynamics employed in the DBM. In the fourth panel from the top, the horizontal line (red) marks the predicted transit velocity of the CME at L1.

3.6. 2010 April 8 CME

In the *SOHO/LASCO* observations, this CME was detected at 04:54 UT on April 8 as a partial halo. The plane-of-sky speed of this CME was 264 km s^{-1} ; the CME decelerated in the LASCO FOV. SECCHI/COR1 A observed this CME in the NE quadrant and COR1 B observed it in the NW quadrant at 03:25 UT on April 8. The CME was accompanied by a B3.7 flare in NOAA AR 11060.

A time–elongation plot (*J*-map) in the ecliptic plane was constructed for this CME. The CME was tracked in the heliosphere up to a 54° elongation angle in *J*-maps constructed from SECCHI A observations. In *J*-maps constructed from SECCHI B observations, it could be tracked up to 44° only. For comparison, planets Earth and Mars are seen at 58° and 48° elongation, respectively, in the HI2 A FOV on April 8. In the HI2 B FOV at this time, the Earth is seen at 54° elongation. The GT scheme is implemented to estimate the distance and propagation direction of the CME in the heliosphere. The estimated propagation direction of the CME is converted to an angle with respect to the Sun–Earth line in the ecliptic plane. Its positive value implies that the CME was moving to the west from the Sun–Earth line while a negative value would mean that the CME was propagating to the east. The obtained kinematics are shown in Figure 15 and the gap in the estimated kinematics for nearly 12 hr is due to the occurrence of a singularity in the triangulation scheme.

We used the drag model with the inputs of a take-off velocity of 550 km s^{-1} , a take-off distance of $167.3 R_\odot$, a take-off date and time of April 10 at 17:07 UT, an ambient solar wind speed of 350 km s^{-1} , and a drag parameter of $0.2 \times 10^{-7} \text{ km}^{-1}$. Using these inputs in the DBM, the predicted arrival time of the CME is 09:45 UT on April 11 and the transit velocity is 511 km s^{-1} at L1. Keeping all the input parameters the same and taking the drag parameter value as $2 \times 10^{-7} \text{ km}^{-1}$ in the DBM, the predicted arrival time of the CME is 12:55 UT on April 11 with a transit speed of 402 km s^{-1} . By extrapolating the second-order polynomial fit of distance, the predicted arrival time of the CME at L1 is 06:32 UT on April 11. With 3D reconstruction of the CME using the tie-pointing technique on SECCHI/COR2 data, the true velocity of the CME leading edge at the true height of $12 R_\odot$ was found to be 478 km s^{-1} at 07:24 UT on April 8. Assuming that the CME speed is constant beyond the COR2 FOV, its predicted arrival time at L1 is 16:35 UT on April 11.

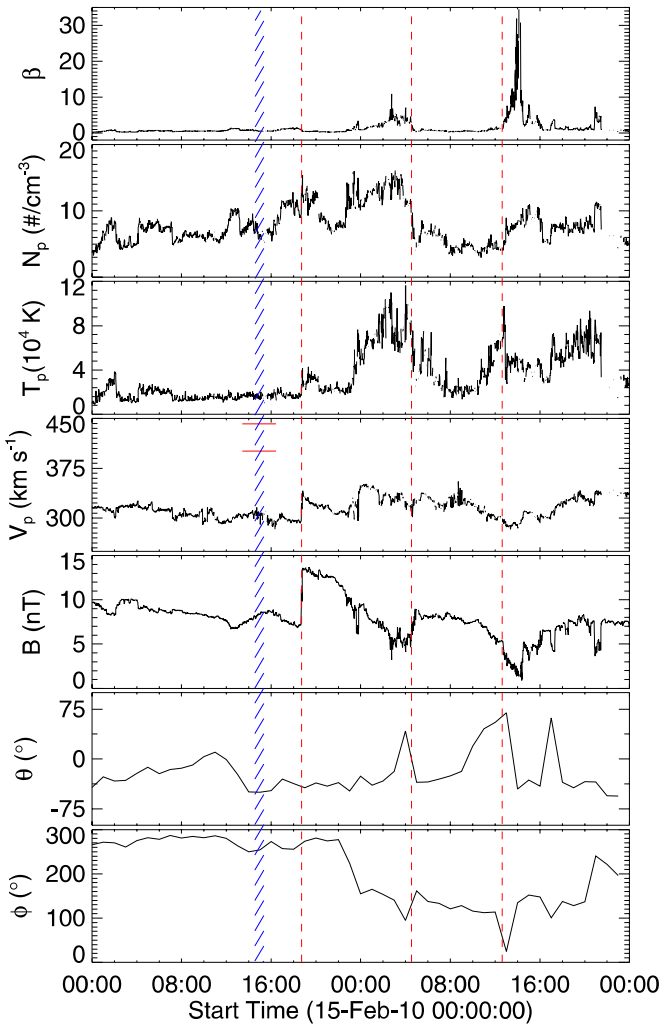


Figure 10. From top to bottom, panels show the plasma beta, proton density, proton temperature, proton velocity, magnitude of magnetic field, latitude and longitude of the magnetic field vector, respectively, corresponding to the CME of 2010 February 12. From the left, the first, second, and third vertical dashed lines (red) mark the arrival time of the shock and the leading and trailing edges of the CME, respectively. The hatched region (blue) marks the interval of the predicted arrival time of the tracked feature. In the fourth panel, horizontal lines (red) mark the predicted velocities of the tracked feature at L1.

(A color version of this figure is available in the online journal.)

By analyzing the in situ data taken nearly at 1AU, the identification of the CME boundary is shown in Figure 16. In this figure, a weak shock or sheath is marked by the first dashed vertical line (red) at 12:44 UT on April 11. Leading and trailing edges of a magnetic cloud are marked by the second and third vertical dashed lines (red) at 02:10 UT and 13:52 UT on April 12, respectively. The blue hatched region shows the predicted arrival time of the CME (with uncertainties) obtained using DBM.

3.7. 2010 October 10 CME

This CME was accompanied by a filament eruption in the southeast quadrant of the solar disk. LASCO on board *SOHO* observed this event at 22:12 UT on October 10 as a slow (projected linear speed $\approx 262 \text{ km s}^{-1}$) and partial halo (angular width $\approx 150^\circ$) CME. The projected speed calculated from SECCHI/COR1 Ahead images was 297 km s^{-1} . The projected speed calculated from SECCHI/COR1 Behind images was

estimated as 328 km s^{-1} . The CME first appeared in the SECCHI/COR1 Ahead FOV at 19:25 UT and then in the SECCHI/COR1 Behind FOV at 20:05 UT.

In the *J*-map, tracking of a feature was feasible at elongations up to 35° and 30° for *STEREO A* and *STEREO B*, respectively. In the *J*-map constructed from images taken by the *STEREO A* spacecraft, there are two nearly horizontal lines and one slanted line in the HI2 FOV starting at elongation angles of 35.2° , 49.4° , and 69.6° , respectively. These lines appeared due to planets Venus, Earth, and Jupiter, respectively, in the HI2 A FOV. In the *J*-map constructed from *STEREO B* images, two horizontal lines that start at elongation angles of 39.8° and 47.9° , respectively, are due to the appearance of planets Venus and Earth in the HI2 B FOV. The kinematics obtained for this CME are shown in Figure 17, where the gap in estimated parameters occurs due to the existence of a singularity in the triangulation scheme.

We used the DBM developed by Vršnak et al. (2013) to estimate the arrival time of the CME. For this event, we used the DBM with a take-off distance of $120.65 R_\odot$, a take-off date and time of 2010 October 13 at 09:33 UT, a take-off velocity of 354 km s^{-1} , an ambient solar wind speed of 350 km s^{-1} , and a drag parameter of $0.2 \times 10^{-7} \text{ km}^{-1}$ to $2 \times 10^{-7} \text{ km}^{-1}$. We obtained its arrival time as 11:40–11:45 UT on October 15 and its transit velocity as $354\text{--}353 \text{ km s}^{-1}$ at L1. By extrapolating the second-order polynomial fit for distance, the predicted arrival time of the CME at L1 is October 14 at 22:53 UT. From the 3D reconstruction of the CME leading edge using the tie-pointing method on SECCHI/COR2 data, the estimated true velocity was found to be 565.8 km s^{-1} at $14.5 R_\odot$ at 06:50 UT on 2010 October 11. Assuming that the speed of CME is constant beyond the COR2 FOV, the predicted arrival time is 02:33 UT on 2010 October 14 at L1 ($\approx 1 \text{ AU}$).

We analyzed the in situ data and identified the CME boundary, which is shown in Figure 18. In this figure, CME sheath arrival is marked by the first vertical dashed line (red) at 04:30 UT on 2010 October 15. The second vertical dashed line (red) marks the trailing edge of the CME sheath region at 01:38 UT on 2010 October 16. The hatched line (blue) marks the predicted arrival time (with uncertainties) obtained using DBM.

3.8. 2010 October 26 CME

This CME was observed by both the *STEREO* spacecraft in COR1 images on October 26. This CME was also observed in *SOHO*/LASCO images around 01:36 UT with an angular width of 83° and had a projected linear speed of 214 km s^{-1} at a position angle of 210° .

The independent elongation angle of a tracked feature from two different vantage points is extracted using *J*-maps. In both *J*-maps, the leading edge of the bright feature has positive slope, revealing that the CME propagation could be tracked up to 28° without ambiguity. For comparison, on October 26 in the HI2 A FOV, planets Venus, Earth, and Jupiter are observed at elongation angles of 38.3° , 48.9° , and 55.8° , respectively. In the HI2 B FOV, planets Venus and Earth are observed at elongation angles of 36.9° and 46.7° , respectively. Figure 19 shows the kinematics of the CME of 2010 October 26, which were obtained by implementing the GT technique (Liu et al. 2010) with the independent elongations estimated from two different view points as inputs. There is a gap in the estimated parameters (Figure 19) due to the existence of a singularity in the triangulation scheme.

We applied the tie-pointing method for 3D reconstruction of a feature along the identified bright blob behind the leading edge

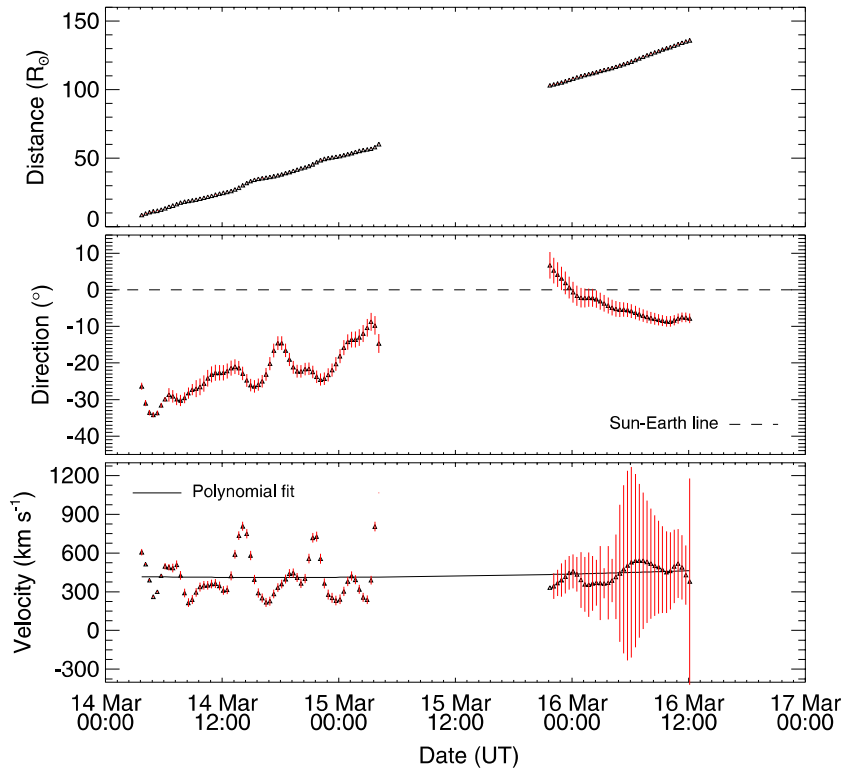


Figure 11. From top to bottom, panels show the distance, propagation direction, and velocity, respectively, of the 2010 March 14 event. For details see the caption to Figure 4.

(A color version of this figure is available in the online journal.)

in both sets of calibrated- and background-subtracted images obtained by SECCHI/COR2. Our goal was to estimate its true kinematics in the COR2 FOV. Estimated latitude and longitude show that the CME is Earth directed. The speed of the CME using 3D reconstruction at the outer edge of the COR2 FOV is about 600 km s^{-1} with an acceleration of 30 m s^{-2} . Assuming that the speed of the CME is constant beyond this distance, the predicted arrival time of the CME at L1 is 07:45 UT on 2010 October 29. We used the DBM with a take-off date and time of 2010 October 28 at 13:57 UT, a take-off distance of $110.5 R_{\odot}$, a take-off velocity of 341 km s^{-1} , an ambient solar wind speed of 350 km s^{-1} , and a drag parameter value of $0.2 \times 10^{-7} \text{ km s}^{-1}$. The resulting CME arrival time is 23:45 UT on 2010 October 30 and the transit speed is 341 km s^{-1} at L1. Keeping all the input parameters same but using a different drag parameter value, $2.0 \times 10^{-7} \text{ km}^{-1}$, the CME arrival time is 23:35 UT on 2010 October 30 and the transit speed is 343 km s^{-1} at L1. The predicted arrival time of the CME at L1, obtained by extrapolating a second-order polynomial fit for distance, is 08:32 UT on October 30.

We analyzed the in situ observations of solar wind taken nearly at 1 AU and the identification of the CME is shown in Figure 20. In this figure, there is a sudden enhancement of density, temperature, and velocity at 10:32 UT on October 30. These changes mark the arrival of a shock, as indicated by the first dashed vertical line (red) from the left. The hatched line (blue) marks the predicted arrival time (with uncertainty) of the CME using DBM. From the left, the second and fourth vertical dashed lines (red) mark the leading and trailing edges of the CME. Leading and trailing edges of a magnetic cloud (Klein & Burlaga 1982; Lepping et al. 1990) are marked by the third and fourth vertical dashed lines (red) at 01:30 and 21:35 UT

November 1, respectively. This region of the CME has a low proton beta (Burlaga et al. 1981; Cane & Richardson 2003), a decrease in proton density (Richardson et al. 2000), a decrease in proton temperature (Gosling et al. 1973), a monotonic decrease in proton velocity (Klein & Burlaga 1982), and an enhanced alpha to proton ratio (Borrini et al. 1982). These properties are also observed in the in situ data in Figure 20.

4. RESULTS AND DISCUSSION

We studied kinematics for eight selected CMEs by implementing the GT technique (Liu et al. 2010) that uses elongation (derived from J -maps) as input. We tracked the positively-inclined bright features in the J -maps that are considered to be enhanced density regions of CMEs moving along the ecliptic. The arrival time of these bright features is expected to match the arrival of the enhanced density features in in situ observations. Therefore, in the present study, we define the actual arrival time of a CME as the time when the first density peak is observed in in situ measurements taken at the L1 point.

We predicted the arrival time (T_{arr}) of CMEs at the L1 point using three different approaches, described in Section 3.1.3. The arrival time predicted from the two different approaches (DBM and polynomial fit) that use inputs of derived parameters from GT with J -maps was compared with the actual arrival time of the enhanced density feature at the L1 point. For each CME studied here, the actual arrival time and errors in the predicted arrival time using these two approaches are shown in Table 1. The predicted arrival time of a CME using DBM is shown in the third column of Table 1, corresponding to the two extreme values of the range of the drag parameter. Predicted transit velocity (v_1) of the CME at L1 is also compared with the actual measured

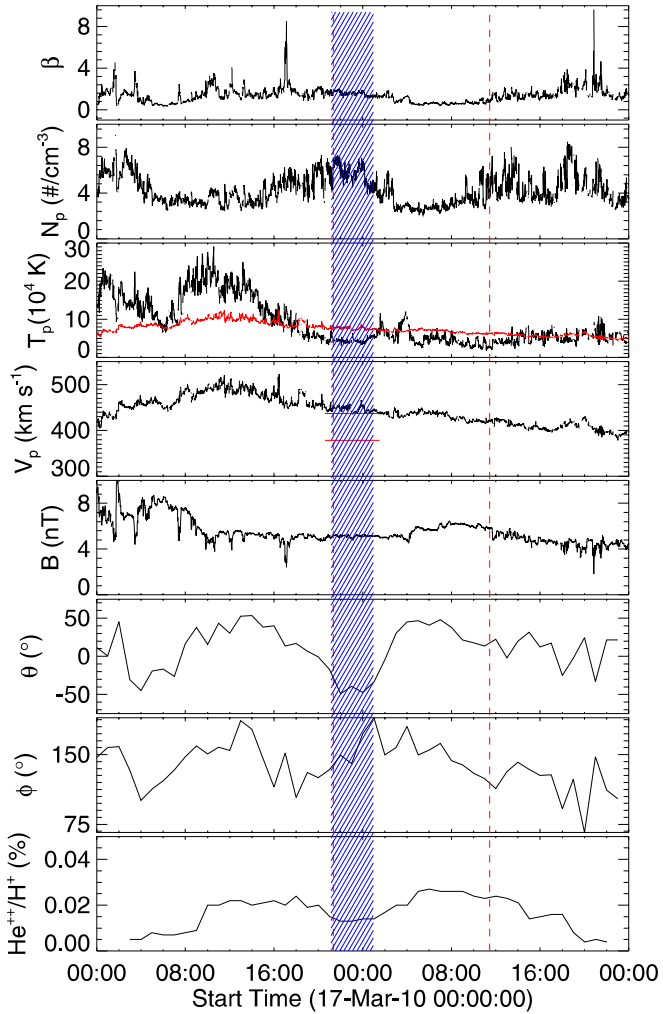


Figure 12. From top to bottom, panels show the plasma beta, proton density, proton temperature, proton velocity, magnitude of magnetic field, latitude and longitude of the magnetic field vector, and the alpha to proton ratio, respectively, corresponding to the CME of 2010 March 14. From the left, the first and second vertical dashed lines (red) mark the arrival time of the CME leading and trailing edges, respectively. The hatched region (blue) marks the interval of the predicted arrival time of the tracked feature. In the third panel from the top, the expected proton temperature is shown as a red curve and in the fourth panel two horizontal lines (red) mark the predicted velocities of the tracked feature at L1.

(A color version of this figure is available in the online journal.)

in situ velocity (fifth column), at the time of the arrival of the enhanced density feature. Negative (positive) values of errors in arrival time indicate that predicted arrival is earlier (later) than the actual arrival time. Negative (positive) values of error in the transit velocity of the CME at L1 indicate that the predicted transit velocity of the CME at L1 is lesser (greater) than the transit velocity measured in situ.

In order to examine the efficacy of the third approach, one must be certain that the arrival time of the tracked feature at L1 is correctly marked. It is generally difficult to mark the actual (reference) arrival time of a remotely observed (in COR2) feature at L1 by analyzing the in situ data. This difficulty arises due to uncertainty in the one-to-one identification of remotely observed structures with in situ observed structures. In previous studies, various authors have adopted different signatures of CMEs near 1 AU as references when correlating remote sensing observations with in situ observations. For instance, in the derivation of the ECA time prediction model, Gopalswamy et al.

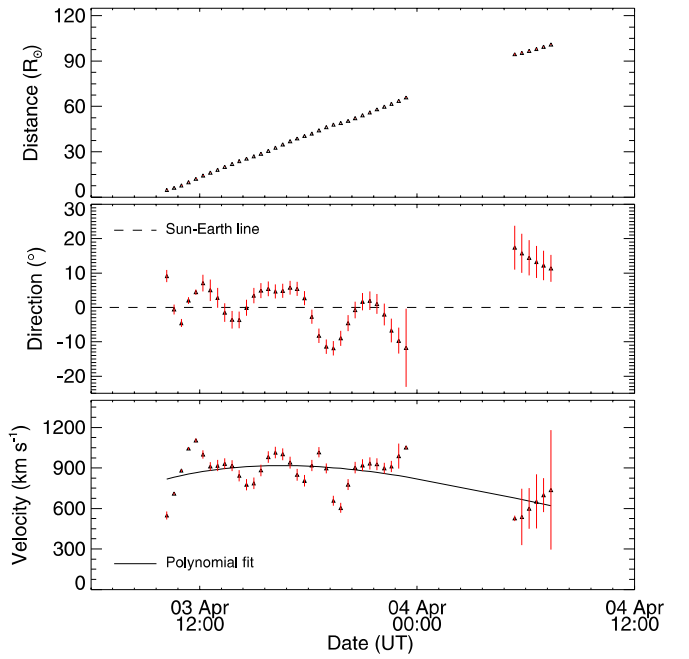


Figure 13. From top to bottom, panels show the distance, propagation direction, and velocity, respectively, of the 2010 April 3 event. For details see the caption to Figure 4.

(A color version of this figure is available in the online journal.)

(2000) adopted the start time of the magnetic cloud and low proton beta ($\beta < 1$) as a reference for the actual arrival time of the CME. In another study, Schwenn et al. (2005), an IP shock was taken as a reliable in situ signature for the arrival of a CME. In the study by Zhang et al. (2003), the minimum Dst index of the associated geomagnetic storm was considered as the ICME arrival time. Kilpua et al. (2012) considered the arrival time of the CME leading edge at in situ spacecraft as the arrival of a CME. In our study, the majority of selected CMEs are slow and do not drive an IP shock. Furthermore, only three events, i.e., 2008 December 12, 2010 April 8, and 2010 October 26, could be categorized as magnetic clouds in in situ measurements. For all the CMEs studied in this paper, except 2010 October 26, we have estimated the true speed of a feature along its leading edge in the COR2 FOV by implementing the tie-pointing method. Also, for all the CMEs, except 2010 October 10, leading and trailing boundaries of the CMEs could be well identified using in situ data. Therefore, for our study we take the CME leading edge in in situ data as a reference for the CME arrival (of a selected feature in COR2) as the most appropriate approach for comparing the predicted arrival time of the CME (selected feature in COR2) with the actual arrival time of the CME leading edge at L1. The error in the predicted arrival time of the CME using true speed (estimated in the COR2 FOV) is shown in Table 2. In this table, the true speed in the COR2 FOV and the measured speed of the CME leading edge at L1 are also shown. In this table, the CME of 2010 October 10 is not included because the CME boundaries could not be identified in in situ data; it seems probable that only the CME flank was encountered by the spacecraft. It would have been possible to confirm the above by discussing multi-point observations of this CME, if the STEREO spacecraft had a smaller separation angle at this time (similar to the study carried out by Kilpua et al. (2011)).

From Tables 1 and 2, it is clear that, in general, a more accurate prediction of CME arrival time is possible using DBM

Table 1
Errors in the Predicted Arrival Time Using Two Approaches

CME Dates	Actual T_{arr} (Peak Density Time) (UT)	Error in Predicted T_{arr} at L1 (hr)		Actual v_1 at L1 (km s $^{-1}$)	Error in Predicted v_1 at L1 (km s $^{-1}$) [$y = 0.2-2.0(10^{-7} \text{ km}^{-1})$]
		Kinematics + Drag-Based Model [$y = 0.2-2.0(10^{-7} \text{ km}^{-1})$]	Distance + Polynomial Fit		
2008 Dec 12	Dec 16 23:50	-3.4 to -3.9	+6.5	356	-25 to -18
2010 Feb 7	Feb 11 02:05	-4.3 to -3.2	-1.2	370	+72 to +23
2010 Feb 12	Feb 15 23:15	-8.7 to -7.9	-7.1	320	+122 to +81
2010 Mar 14	Mar 17 21:45	-0.6 to +3.2	-5.4	453	-16 to -75
2010 Apr 3	Apr 5 12:00	+5.5	-3.0	720	-96
2010 Apr 8	Apr 11 14:10	-4.4 to -1.2	-7.6	426	+85 to -24
2010 Oct 10	Oct 15 06:05	+5.5 to +5.6	-7.2	300	+54 to +53
2010 Oct 26	Oct 31 03:30	-3.7 to -4.0	-18.9	365	-24 to -22

Notes. The actual arrival time and the transit velocity of the tracked feature at the L1 point are shown in Columns 2 and 5, respectively. Errors in the predicted arrival time using two approaches are shown in Columns 3 and 4 and errors in the predicted transit velocity in Column 6.

Table 2
Errors in the Predicted Arrival Time Estimated Using the True Velocity in the COR2 FOV

CME Dates	Actual Arrival Time (UT) of CME Leading Edge at L1	Error in Predicted Arrival Time	Measured Velocity of CME Leading Edge at L1	Velocity (km s^{-1}) in the COR2 FOV
2008 Dec 12	Dec 17 04:39	-26.9	365	453
2010 Feb 7	Feb 11 12:47	-21.8	360	480
2010 Feb 12	Feb 16 04:32	-41.5	310	867
2010 Mar 14	Mar 17 21:19	+27	450	335
2010 Apr 3	Apr 5 13:43	-2.3	800	816
2010 Apr 8	Apr 12 02:10	-9.5	410	478
2010 Oct 26	Oct 31 06:30	-46.7	365	600

Notes. The second column shows the actual arrival time at L1, the third column shows errors in the predicted arrival time, the fourth column shows the CME leading edge velocity measured at the L1 point by in situ spacecraft, and the fifth column shows the true velocity in the COR2 FOV.

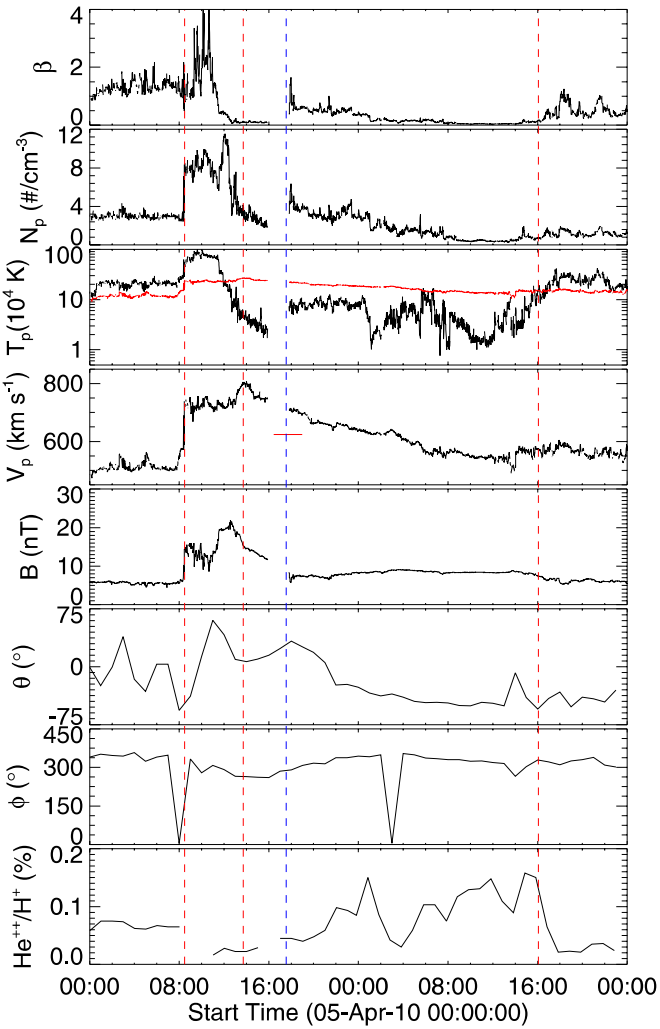


Figure 14. From top to bottom, panels show the plasma beta, proton density, proton temperature, proton velocity, magnitude of magnetic field, latitude and longitude of the magnetic field vector, and the alpha to proton ratio, respectively, corresponding to the CME of 2010 April 3. From the left, the first, second, and fourth vertical dashed lines (red) mark the arrival time of the shock and the leading and trailing edges of the CME, respectively. The third vertical dashed line (blue) marks the predicted arrival time of the tracked feature. In the third panel from the top, the expected proton temperature is shown as a red curve and in the fourth panel a horizontal line (red) marks the predicted velocities of the tracked feature at L1.

(A color version of this figure is available in the online journal.)

combined with kinematics estimated from the GT technique. It is also obvious from Table 2 that, for the 2010 April 3 and April 8 CMEs, the implementation of the tie-pointing technique provides a more accurate arrival time prediction. In these cases, CME transit speeds at L1 are approximately equal to the measured CME speeds in the COR2 FOV. This result shows that the speeds of the CMEs did not change significantly during their propagation in the heliosphere. Therefore, in these particular cases, the observed CME speeds in the COR2 FOV is sufficient to predict their arrival times near 1 AU with reasonably good accuracy. Our analysis of the April 3 CME shows that CME speed is partly governed by the high-speed stream from a coronal hole located in a geoeffective location on the Sun. The estimated speed ($\approx 816 \text{ km s}^{-1}$) of the April 3 CME in the COR2 FOV and its measured speed ($\approx 800 \text{ km s}^{-1}$) in situ highlight the weak drag force experienced by this CME throughout its journey up to 1 AU. Therefore, the CME speed did not tend

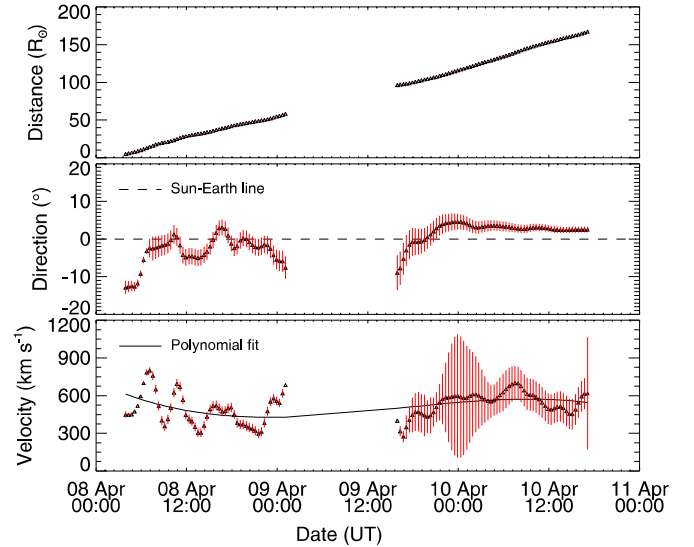


Figure 15. From top to bottom, panels show the distance, propagation direction, and velocity, respectively, of the 2010 April 8 event. For details see the caption to Figure 4.

(A color version of this figure is available in the online journal.)

toward the ambient solar wind speed even up to 1 AU. These findings are in good agreement with the results of Temmer et al. (2011).

Predicting arrival time by extrapolating the fitted second-order polynomial for estimated distance is also better than the prediction made using only the true speed estimated in the COR2 FOV. The decelerating trend of the 2008 December 12 CME in the inner heliosphere is in good agreement with the results of Liu et al. (2010). Using extrapolation, the error in the predicted arrival time is also less if a CME is tracked up to very large distances in the heliosphere (using HI), as in the case of the 2010 February 7 CME where the *J*-map allowed tracking of CME features at elongations up to nearly 50° ($\approx 170 R_\odot$). The high-speed ($\approx 867 \text{ km s}^{-1}$) CME of 2010 February 12 shows a significant, continuous deceleration in the heliosphere. This is in agreement with the results of previous studies that demonstrate that the drag force plays an important role in shaping CME dynamics (Lindsay et al. 1999; Gopalswamy et al. 2001; Manoharan 2006; Vršnak & Žic 2007).

In our study, CMEs could be tracked in HI images up to a large elongation angle ($\approx 35^\circ$). However, relating the tracked feature to features observed *in situ* is often challenging. Though in the GT technique, we assume that the same enhanced density structure is tracked using *J*-maps from both *STEREO* spacecraft. We also assume that the same structure appears in each consecutive image. These assumptions are not truly valid for observed CMEs. Even if these assumptions are thought to be true, it is possible that single *in situ* spacecraft would be unable to sample the tracked feature. In this situation, which is worse, relating a remotely observed tracked feature with *in situ* observations will lead to an incorrect interpretation. Since, the location of an *in situ* spacecraft with respect to the CME structure determines which part of the CME will be visible by the *in situ* spacecraft, it may be more appropriate to also take into account the geometry of CMEs in the GT scheme. In the present work, we made the *J*-map along the ecliptic plane as the estimated velocity in this plane is more suitable than radial velocity at other position angles for estimating the arrival time of CMEs at the L1 point. But, even in the ecliptic plane, the

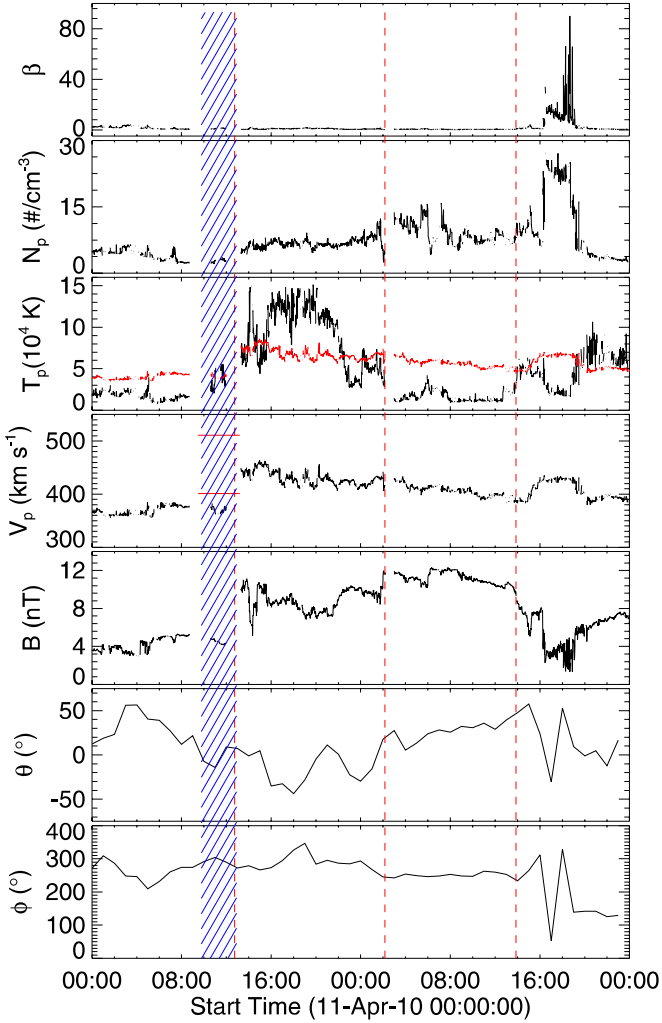


Figure 16. From top to bottom, panels show the plasma beta, proton density, proton temperature, magnitude of magnetic field, and latitude and longitude of the magnetic field vector, respectively, corresponding to the CME of 2010 April 8. From the left, the first, second, and third vertical dashed lines (red) mark the arrival time of the sheath and the leading and trailing edges of a magnetic cloud, respectively. The hatched region (blue) marks the interval of the predicted arrival time of the tracked feature. In the third panel from the top, the expected proton temperature is shown as a red curve and in the fourth panel two horizontal lines (red) mark the predicted velocities of the tracked feature at L1.

(A color version of this figure is available in the online journal.)

J-map gives information about only a part of the CME structure that has different velocities at different longitudes. Different parts of a CME traverse a fixed radial distance from the Sun in different times. The time is minimized for the apex of a CME (Schwenn et al. 2005). If the tracked feature happens to be at the apex of a CME moving in a different direction (longitude) from the Sun–L1 line, then the predicted arrival time of this CME using the estimated speed of the tracked feature will be earlier than the actual arrival time of the CME at the L1 point. Therefore, to obtain the actual arrival time and transit velocity of a CME passing the in situ spacecraft, it is necessary to take into account the propagation direction of the tracked feature. Möstl et al. (2011) showed that the speed of a CME flank measured at a given angle θ to the CME apex is reduced by a factor of $\cos(\theta)$ for a circular geometry of the CME. Therefore, it seems reasonable that the transit speed measured in situ and the arrival time of the CME at L1 should be compared with

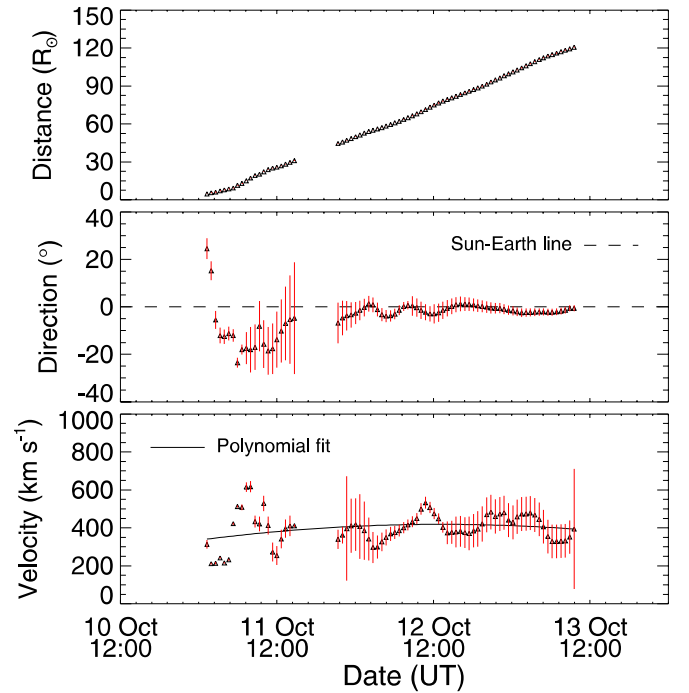


Figure 17. From top to bottom, panels show the distance, propagation direction, and velocity, respectively, of the 2010 October 10 event. For details see the caption to Figure 4.

(A color version of this figure is available in the online journal.)

the corresponding corrected speed of the tracked feature along the Sun–L1 line and the arrival time, respectively. However, we note that if the apex of the CME moves with a linear speed of 400 km s^{-1} at 10° to the Sun–L1 line, the correction in the actual arrival time of the CME at L1 is only approximately 2 hr for a fixed distance of nearly 1 AU. It seems appropriate to also take the geometry of CMEs into account in the triangulation scheme. However, idealistic assumptions about geometry also are far from the real structure. Further, CME shapes can be distorted in the heliosphere by solar wind, IP shocks, and CME interactions. Therefore, one needs to be cautious as assumptions about geometry may result in new sources of errors.

In spite of various assumptions made in the DBM (Vršnak et al. 2013) and in the GT technique (Liu et al. 2010), the predicted arrival times of CMEs are found within acceptable error. It must be mentioned here that the estimated velocity profiles of the selected CMEs show small apparent accelerations and decelerations for few hours that do not seem to be real. We believe that these may be due to errors in the manual tracking of a CME feature using *J*-maps and the extraction of the elongation angles. In the kinematics plot, we have shown the error bars with vertical red lines. However, these do not denote the actual errors in the triangulation scheme, but are representative of the sensitivity of the technique to elongation uncertainties (Liu et al. 2010). Considering that the elongation angles determined for each pixel in level 0 data for COR2 and level 2 data for HI1 and HI2 are quite accurate, the minimum uncertainty in the elongation will be determined by the resolution in elongation that is used to construct the *J*-maps. However, as mentioned above, the actual error in this technique owes to the manual error in tracking the bright points using *J*-maps. The assessment of this error is possible by repeating the manual tracking of a feature several times and comparing the derived parameters. One should also ensure that the same feature is tracked continuously

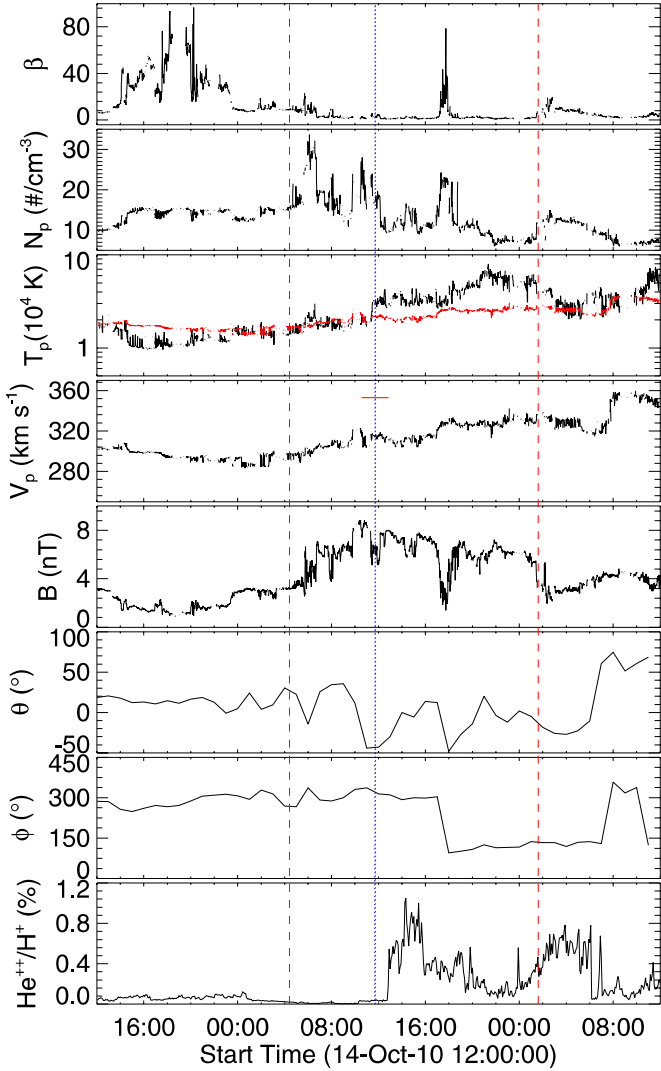


Figure 18. From top to bottom, panels show the plasma beta, proton density, proton temperature, magnitude of magnetic field, latitude and longitude of the magnetic field vector, and the alpha to proton ratio, respectively, corresponding to the CME of 2010 October 10. From the left, the first and second vertical dashed lines (red) mark the arrival time of the leading and trailing edges of the CME sheath, respectively. The hatched line (blue) marks the interval of the predicted arrival time of the tracked feature. In the third panel from the top, the expected proton temperature is shown as a red curve and in the fourth panel two horizontal lines (red) mark the predicted velocities of the tracked feature at L1.

(A color version of this figure is available in the online journal.)

in the J -maps. This is often difficult due to different sensitivities of the COR2, HI1, and HI2 imaging instruments, which cover a wide range of elongation angles. The actual sources of error in the GT technique are inherent in the assumption that the CME feature is a single point and the same point is being tracked continuously from both twin *STEREO* spacecraft. If the assumption fails (likely at larger elongations) at some segment of journey in the IP medium, the CME kinematics will not be correctly estimated.

We also note that the density distribution along the line of sight is not well known, as we project the 3D structure of CME features onto a 2D image. Relating remote sensing observations to in situ measurements of CMEs is often uncertain, because the bright feature observed in J -maps is due to the contribution of intensity along the entire depth of the line of sight but *ACE*

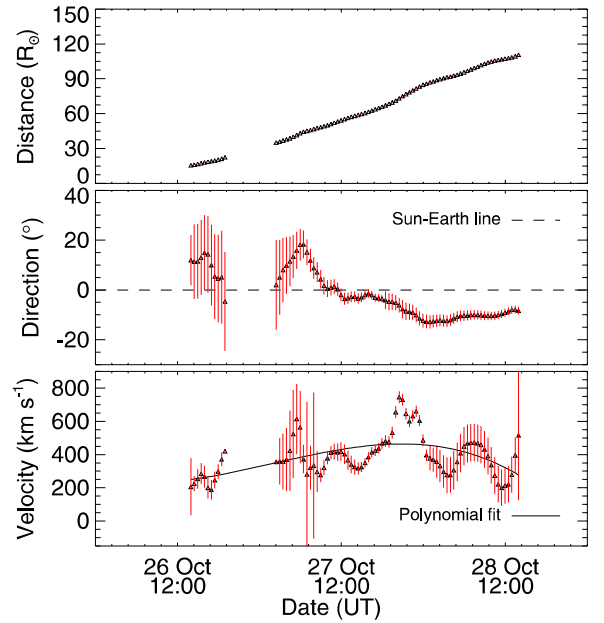


Figure 19. From top to bottom, panels show the distance, propagation direction, and velocity, respectively, of the 2010 October 26 event. For details see the caption to Figure 4.

(A color version of this figure is available in the online journal.)

or *WIND* density measurements near 1 AU are only along the Sun–Earth line. In spite of these constraints on observations and assumptions in implemented techniques, our study shows a fair agreement in relating remotely observed features with in situ measurements. We track the CMEs up to large distances in the heliosphere. The efficacy of any forecasting scheme for CME arrival time must be validated with real time data so that the results are unbiased. Furthermore, we aim to implement other techniques, e.g., fixed ϕ (Kahler & Webb 2007), harmonic mean fitting (Lugaz et al. 2009), triangulation with harmonic mean (Lugaz et al. 2010), and self-similar expansion method (Davies et al. 2012), on these CMEs to ascertain and compare the kinematics obtained in the heliosphere.

5. SUMMARY

We have studied the kinematics of eight CMEs by exploiting the *STEREO* COR2 and HI observations. Speeds of the selected CMEs in our study range from low ($\approx 335 \text{ km s}^{-1}$) to high ($\approx 870 \text{ km s}^{-1}$) in the coronagraphic (COR2) FOV. We obtained a good agreement (within $\approx 100 \text{ km s}^{-1}$) between the speed calculated using the tie-pointing method of 3D reconstruction and the speed derived by implementing the GT technique using J -maps in the COR2 FOV. The difference in the speeds using the two different techniques can occur because of the estimation of speeds of different features at different latitudes.

Based on our prediction of the arrival times of CMEs at L1 using three different approaches, our study reveals that use of the GT technique on HI data combined with DBM gives a better prediction of the CME arrival time. Error values range from 3–9 hr and transit velocities near 1 AU have an error ranging from $25\text{--}120 \text{ km s}^{-1}$. Our study also shows that using the true speed of CMEs determined at the farthest point in the COR2 FOV and assuming that the speed remains constant for the remaining distance, i.e., up to 1 AU, may not be sufficient to predict the CME arrival times accurately for a majority of events. Also, it is worth mentioning that a small change in the

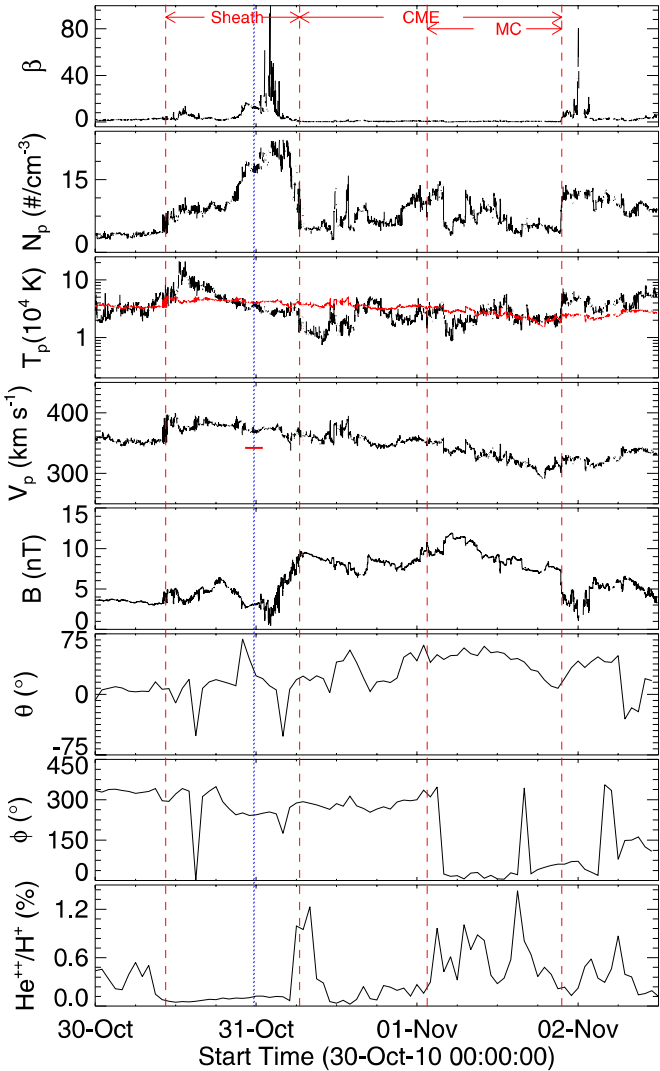


Figure 20. From top to bottom, panels show the plasma beta, proton density, proton temperature, proton velocity, magnitude of magnetic field, latitude and longitude of the magnetic field vector, and the alpha to proton ratio, respectively, corresponding to the CME of 2010 October 26. From the left, the first, second, third, and fourth vertical dashed lines (red) mark the arrival time of the shock, the trailing edge of the CME sheath, and the leading edge and the trailing edge of a magnetic cloud, respectively. The hatched line (blue) marks the interval of the predicted arrival time of the tracked feature. In the third panel from the top, the expected proton temperature is shown as a red curve and in the fourth panel two horizontal lines (red) mark the predicted velocities of the tracked feature at L1.

(A color version of this figure is available in the online journal.)

estimated speed in the COR2 FOV may result in a large variation in the predicted arrival time near 1 AU. This variation may be due to the large distance between the COR2 FOV and near 1 AU. For comparison, a change in the estimated speed from 400 to 450 km s^{-1} results in a difference in the estimated arrival time of 10.5 hr near 1 AU. However, for fast CMEs, this variation in arrival time using slightly different estimated true speeds will be minimized. Our study shows that exploiting wide angle imaging data from the HI with the GT technique combined with DBM helps one to understand the relationship between remote sensing and in situ observations, CME acceleration and deceleration beyond the COR2 FOV, and the role of the ambient solar wind in depth. Our technique also reveals the non-radial motion of CMEs even far from the Sun from the estimation of the propagation direction.

We thank J. A. Davies, Anand D. Joshi, and Y. Liu for their support with programming in the preparation of *J*-maps and for helpful discussions on singularities in the geometric triangulation technique. We thank the *STEREO/SECCHI*, *ACE* and *WIND* teams for their open data policy. The work by N.S. partially contributes to the research for the European Union Seventh Framework Programme (FP7/2007-2013) for the Coronal Mass Ejections and Solar Energetic Particles (COMESEP) project under Grant Agreement No. 263252.

REFERENCES

- Andrews, M. D., Wang, A.-H., & Wu, S. T. 1999, *SoPh*, **187**, 427
 Billings, D. E. 1966, *A Guide to the Solar Corona* (San Diego, CA: Academic)
 Borri尼, G., Gosling, J. T., Bame, S. J., & Feldman, W. C. 1982, *JGR*, **87**, 7370
 Boursier, Y., Lamy, P., & Llebaria, A. 2009, *SoPh*, **256**, 131
 Brueckner, G. E., Howard, R. A., Koomen, M. J., et al. 1995, *SoPh*, **162**, 357
 Burlaga, L., Sittler, E., Mariani, F., & Schwenn, R. 1981, *JGR*, **86**, 6673
 Byrne, J. P., Maloney, S. A., McAteer, R. T. J., Rejojo, J. M., & Gallagher, P. T. 2010, *NatCo*, **1**, 74
 Cane, H. V., & Richardson, I. G. 2003, *JGRA*, **108**, 1156
 Cargill, P. J. 2004, *SoPh*, **221**, 135
 Colaninno, R. C., & Vourlidas, A. 2009, *ApJ*, **698**, 852
 Davies, J. A., Harrison, R. A., Perry, C. H., et al. 2012, *ApJ*, **750**, 23
 Davies, J. A., Harrison, R. A., Rouillard, A. P., et al. 2009, *GeoRL*, **36**, 2102
 Davis, C. J., Davies, J. A., Lockwood, M., et al. 2009, *GeoRL*, **36**, 8102
 Dryer, M. 1994, *SSRv*, **67**, 363
 Dryer, M., Smith, Z., Fry, C. D., et al. 2004, *SpWea*, **2**, 9001
 Dungey, J. W. 1961, *PhRvL*, **6**, 47
 Echer, E., Gonzalez, W. D., Tsurutani, B. T., & Gonzalez, A. L. C. 2008, *JGRA*, **113**, 5221
 Eyles, C. J., Harrison, R. A., Davis, C. J., et al. 2009, *SoPh*, **254**, 387
 Feng, X. S., Zhang, Y., Sun, W., et al. 2009, *JGRA*, **114**, 1101
 Gopalswamy, N., Lara, A., Lepping, R. P., et al. 2000, *GeoRL*, **27**, 145
 Gopalswamy, N., Lara, A., Manoharan, P. K., & Howard, R. A. 2005, *AdSpR*, **36**, 2289
 Gopalswamy, N., Yashiro, S., Kaiser, M. L., Howard, R. A., & Bougeret, J.-L. 2001, *JGR*, **106**, 29219
 Gosling, J. T., Bame, S. J., McComas, D. J., & Phillips, J. L. 1990, *GeoRL*, **17**, 901
 Gosling, J. T., McComas, D. J., Phillips, J. L., & Bame, S. J. 1991, *JGR*, **96**, 7831
 Gosling, J. T., Pizzo, V., & Bame, S. J. 1973, *JGR*, **78**, 2001
 Harrison, R. A., Davies, J. A., Möstl, C., et al. 2012, *ApJ*, **750**, 45
 Howard, R. A., Moses, J. D., Vourlidas, A., et al. 2008, *SSRv*, **136**, 67
 Howard, T. A., & Tappin, S. J. 2009a, *SSRv*, **147**, 31
 Howard, T. A., & Tappin, S. J. 2009b, *SSRv*, **147**, 89
 Hundhausen, A. J., Sawyer, C. B., House, L., Illing, R. M. E., & Wagner, W. J. 1984, *JGR*, **89**, 2639
 Inhester, B. 2006, arXiv:[astro-ph/0612649](https://arxiv.org/abs/astro-ph/0612649)
 Kahler, S. W., & Webb, D. F. 2007, *JGRA*, **112**, 9103
 Kaiser, M. L., Kucera, T. A., Davila, J. M., et al. 2008, *SSRv*, **136**, 5
 Kilpua, E. K. J., Jian, L. K., Li, Y., Luhmann, J. G., & Russell, C. T. 2011, *JASTP*, **73**, 1228
 Kilpua, E. K. J., Mierla, M., Rodriguez, L., et al. 2012, *SoPh*, **279**, 477
 Klein, L. W., & Burlaga, L. F. 1982, *JGR*, **87**, 613
 Lara, A., & Borgazzi, A. I. 2009, in IAU Symp. 257, Universal Heliophysical Processes, ed. N. Gopalswamy & D. F. Webb (Cambridge: Cambridge Univ. Press), 287
 Leblanc, Y., Dulk, G. A., & Bougeret, J.-L. 1998, *SoPh*, **183**, 165
 Lepping, R. P., Burlaga, L. F., & Jones, J. A. 1990, *JGR*, **95**, 11957
 Lindsay, G. M., Luhmann, J. G., Russell, C. T., & Gosling, J. T. 1999, *JGR*, **104**, 12515
 Liu, Y., Davies, J. A., Luhmann, J. G., et al. 2010, *ApJL*, **710**, L82
 Liu, Y., Luhmann, J. G., Bale, S. D., & Lin, R. P. 2011, *ApJ*, **734**, 84
 Liu, Y. D., Luhmann, J. G., Möstl, C., et al. 2012, *ApJL*, **746**, L15
 Lopez, R. E. 1987, *JGR*, **92**, 11189
 Lopez, R. E., & Freeman, J. W. 1986, *JGR*, **91**, 1701
 Lugaz, N., Farrugia, C. J., Davies, J. A., et al. 2012, *ApJ*, **759**, 68
 Lugaz, N., Hernandez-Chapak, J. N., Roussev, I. I., et al. 2010, *ApJ*, **715**, 493
 Lugaz, N., Vourlidas, A., & Roussev, I. I. 2009, *AnGeo*, **27**, 3479
 Maloney, S. A., & Gallagher, P. T. 2010, *ApJL*, **724**, L127
 Manchester, W. B., Gombosi, T. I., Roussev, I., et al. 2004, *JGRA*, **109**, 2107
 Manoharan, P. K. 2006, *SoPh*, **235**, 345
 Mierla, M., Davila, J., Thompson, W., et al. 2008, *SoPh*, **252**, 385

- Mierla, M., Inhester, B., Marqué, C., et al. 2009, *SoPh*, **259**, 123
- Moran, T. G., & Davila, J. M. 2004, *Sci*, **305**, 66
- Möstl, C., Rollett, T., Lugaz, N., et al. 2011, *ApJ*, **741**, 34
- Odstrcil, D., & Pizzo, V. J. 1999, *JGR*, **104**, 483
- Odstrcil, D., Riley, P., & Zhao, X. P. 2004, *JGRA*, **109**, 2116
- Ogilvie, K. W., Chornay, D. J., Fritzenreiter, R. J., et al. 1995, *SSRv*, **71**, 55
- Richardson, I. G., Berdichevsky, D., Desch, M. D., & Farrugia, C. J. 2000, *GeoRL*, **27**, 3761
- Richardson, I. G., & Cane, H. V. 2010, *SoPh*, **264**, 189
- Richardson, I. G., Cliver, E. W., & Cane, H. V. 2001, *GeoRL*, **28**, 2569
- Rouillard, A. P., Savani, N. P., Davies, J. A., et al. 2009, *SoPh*, **256**, 307
- Schwenn, R., dal Lago, A., Huttunen, E., & Gonzalez, W. D. 2005, *AnGeo*, **23**, 1033
- Sheeley, N. R., Walters, J. H., Wang, Y.-M., & Howard, R. A. 1999, *JGR*, **104**, 24739
- Sheeley, N. R., Jr., Wang, Y.-M., Hawley, S. H., et al. 1997, *ApJ*, **484**, 472
- Smith, Z. K., Dryer, M., McKenna-Lawlor, S. M. P., et al. 2009, *JGRA*, **114**, 5106
- Stone, E. C., Frandsen, A. M., Mewaldt, R. A., et al. 1998, *SSRv*, **86**, 1
- Tappin, S. J. 1987, *P&SS*, **35**, 271
- Temmer, M., Rollett, T., Möstl, C., et al. 2011, *ApJ*, **743**, 101
- Thernisien, A., Vourlidas, A., & Howard, R. A. 2009, *SoPh*, **256**, 111
- Thompson, W. T. 2009, *Icar*, **200**, 351
- Vourlidas, A., & Howard, R. A. 2006, *ApJ*, **642**, 1216
- Vourlidas, A., Subramanian, P., Dere, K. P., & Howard, R. A. 2000, *ApJ*, **534**, 456
- Vršnak, B., & Gopalswamy, N. 2002, *JGRA*, **107**, 1019
- Vršnak, B., & Žic, T. 2007, *A&A*, **472**, 937
- Vršnak, B., Žic, T., Falkenberg, T. V., et al. 2010, *A&A*, **512**, A43
- Vršnak, B., Žic, T., Vrbanec, D., et al. 2013, *SoPh*, **285**, 295
- Webb, D. F., & Howard, T. A. 2012, *LRSP*, **9**, 3
- Wood, B. E., Karovska, M., Chen, J., et al. 1999, *ApJ*, **512**, 484
- Xie, H., Ofman, L., & Lawrence, G. 2004, *JGRA*, **109**, 3109
- Yashiro, S., Gopalswamy, N., Michalek, G., et al. 2004, *JGRA*, **109**, 7105
- Zhang, J., Dere, K. P., Howard, R. A., & Bothmer, V. 2003, *ApJ*, **582**, 520
- Zhang, J., Richardson, I. G., Webb, D. F., et al. 2007, *JGRA*, **112**, 10102
- Zhao, X. 1992, *JGR*, **97**, 15051
- Zurbuchen, T. H., & Richardson, I. G. 2006, *SSRv*, **123**, 31